Journal of General Physiology

ARTICLE

Different fluorescent labels report distinct components of spHCN channel voltage sensor movement

Magdalena N. Wojciechowski[1,3], Chaseley E. McKenzie[1], Andrew Hung[2], Alibek Kuanyshbek[1], Ming S. Soh[1], Christopher A. Reid[1], and Ian C. Forster[1]

We used voltage clamp fluorometry to probe the movement of the S4 helix in the voltage-sensing domain of the sea urchin HCN channel (spHCN) expressed in *Xenopus* oocytes. We obtained markedly different fluorescence responses with either ALEXA-488 or MTS-TAMRA covalently linked to N-terminal Cys332 of the S4 helix. With hyperpolarizing steps, ALEXA-488 fluorescence increased rapidly, consistent with it reporting the initial inward movement of S4, as previously described. In contrast, MTS-TAMRA fluorescence increased more slowly and its early phase correlated with that of channel opening. Additionally, a slow fluorescence component that tracked the development of the mode shift, or channel hysteresis, could be resolved with both labels. We quantitated this component as an increased deactivation tail current delay with concomitantly longer activation periods and found it to depend strongly on the presence of K^+ ions in the pore. Using collisional quenching experiments and structural predictions, we established that ALEXA-488 was more exposed to solvent than MTS-TAMRA. We propose that components of S4 movement during channel activation can be kinetically resolved using different fluorescent probes to reveal distinct biophysical properties. Our findings underscore the need to apply caution when interpreting voltage clamp fluorometry data and demonstrate the potential utility of different labels to interrogate distinct biophysical properties of voltage-gated membrane proteins.

Introduction

Hyperpolarization-activated, cyclic nucleotide-gated (HCN) channels are responsible for cardiac rhythmicity and neuronal excitability (for review see Biel et al., 2009; Wahl-Schott and Biel, 2009). They are permeable to Na^+ and K^+ ions and are modulated by intracellular cAMP. As members of the superfamily of voltage-gated potassium (K_v) channels that all share a common tetrameric structure, each HCN subunit comprises a voltage-sensing domain (VSD) containing positively charged residues in the S4 helix that sense the membrane potential, a pore domain (PD), and an intracellular cyclic nucleotide-binding domain (Fig. 1 A). Whereas most K_v channels open at depolarizing potentials, HCN channels, like KAT1 channels (e.g., Clark et al., 2020), open at hyperpolarizing potentials, a property that is crucial for their physiological roles. Together with the depolarization-gated hERG (human ether-à-go-go-related gene; e.g., $K_v11.1$) and ether-à-go-go-related gene (e.g., $K_v10.1$) channels, HCN channels also differ structurally from most other K_v channels, whereby their tetrameric subunit assembly does not involve domain swapping of the PD and VSDs of adjacent subunits (Flynn and Zagotta, 2018; Lee and MacKinnon, 2017; Wu et al., 2023; Clark et al., 2020; Wang and MacKinnon, 2017). This architectural difference underscores the specific nature of VSD-PD coupling in domain-swapped versus non-domain-swapped channels. In the former, the covalent linkage between S4 and S5 appears to be crucial in achieving a tight coupling between voltage sensor and pore opening, whereas in the latter (e.g., HCN channels), non-covalent interactions between adjacent sites in S5 and S6 are assumed to play a critical role (Fig. 1 A) (e.g., Flynn and Zagotta, 2018; Hung et al., 2021; Ramentol et al., 2020; Wu et al., 2021; Elbahnsi et al., 2023; Cowgill et al., 2019). Our current understanding of HCN channel voltage-dependent activation comes from several decades of studies using electrophysiological and fluorometric techniques as well as more recent structural modeling predictions. Channel opening, induced by a rapid hyperpolarization of the membrane potential, is initiated by an inward fast movement of the S4 helix of the VSD (Dai

---

[1]Florey Institute of Neuroscience and Mental Health, Parkville, Australia; [2]School of Science, STEM College, RMIT University, Melbourne, Australia; [3]Institut für Pharmazeutische und Medizinische Chemie, Pharmacampus, Universität Münster, Münster, Germany.

Correspondence to Ian C. Forster: ian.forster@florey.edu.au; Christopher A. Reid: christopher.reid@florey.edu.au.

Rockefeller University Press
J. Gen. Physiol. 2024 Vol. 156 No. 8 e202413559
https://doi.org/10.1085/jgp.202413559

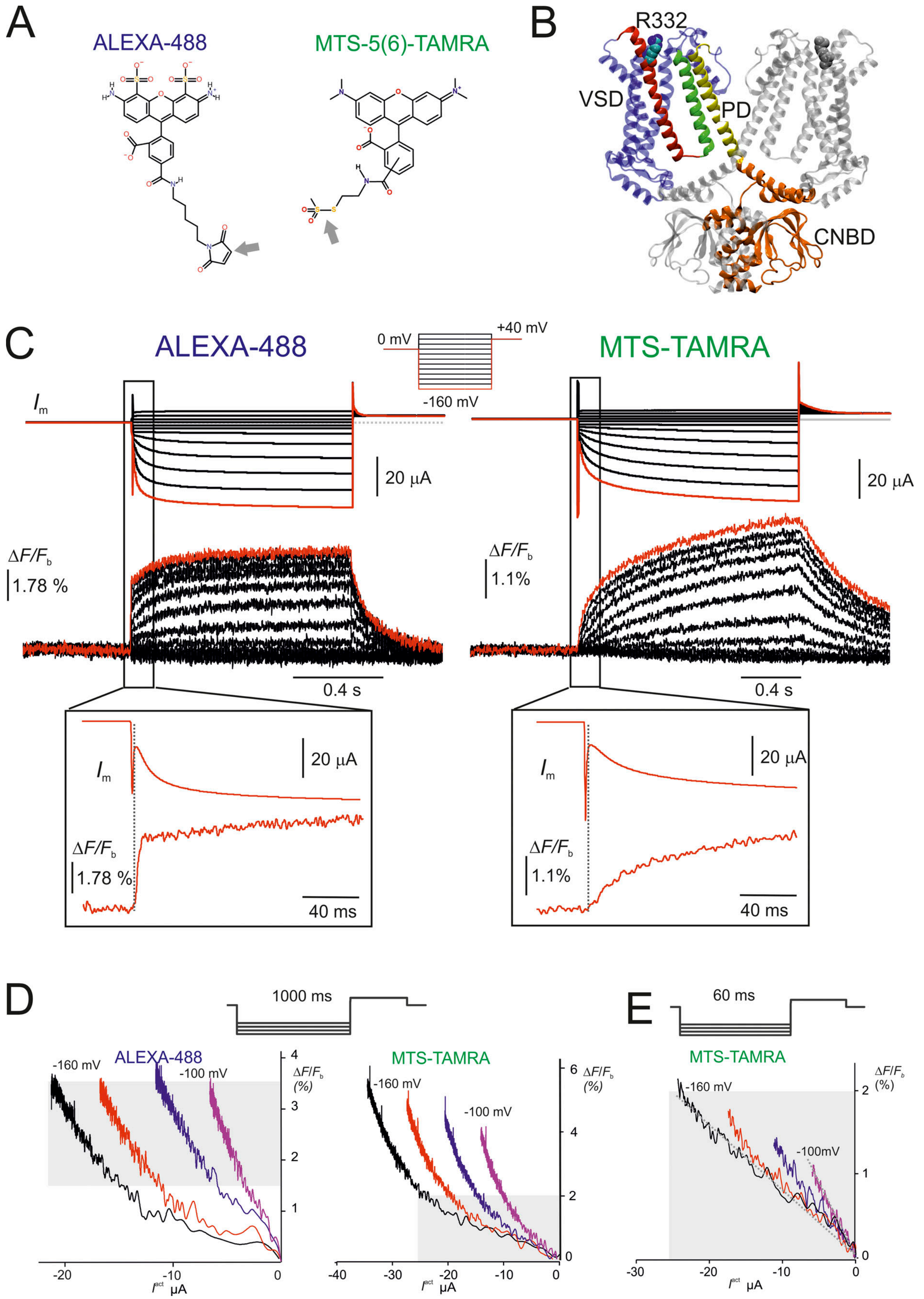

Figure 1. **Distinct voltage-dependent fluorescence changes by labeling spHCN^{R332C} with ALEXA-488 or MTS-TAMRA (mixed isomer). (A)** Chemical structures of the fluorophores used in this study. Arrows indicate site of thiol-maleimide conjugation (ALEXA-488) or S-S cleavage of MTS group (MTS-5(6)-

TAMRA). **(B)** The predicted position of the labeling site R332 is shown in the cartoon rendering of two subunits of spHCN in the closed (depolarized) conformation with main functional components for one subunit highlighted (S1–3: blue; S4: red; S5: yellow; S6:green). CNBD, cyclic nucleotide binding domain. **(C)** Representative recordings of membrane current (I_m, upper panels) and simultaneous fluorescence (ΔF, lower panels) for ALEXA-488–labeled oocyte (left) and MTS-TAMRA–labeled oocyte (right) in response to the voltage step protocol shown. Oocytes were from the same donor frog recorded on consecutive days. Boxed regions expanded (×10) for voltage steps to −160 mV highlight the initial fast ΔF for ALEXA-488 labeling. The vertical dashed lines indicate the approximate end of the capacitive charging phase. ΔF shown as percentage of background fluorescence. Current and fluorescence were low-pass filtered at 400 Hz. **(D)** Parametric plots of ΔF and activating currents (I^{act}) for representative oocytes labeled with either ALEXA-488 (left panel) or MTS-TAMRA (right panel) for four hyperpolarizing potentials from −100 to −160 mV in 20-mV intervals. For the ALEXA-488 data, gray shading indicates region ∼60 ms after step onset, for which I^{act} and ΔF appear to correlate. For the MTS-TAMRA data, the initial 60 ms is shaded and expanded in C. **(E)** MTS-TAMRA data for the same oocyte as in B but using a 60-ms test pulse with the same potentials. Gray marked zone corresponds to same area in B (right panel). Superimposed lines highlight linear relation between early phase of ΔF and I^{act} for MTS-TAMRA labeling for −100 and −160 mV.

et al., 2019), followed by the development of a helix break in S4 that permits re-orientation of the S5 and S6 domains to allow pore opening through rotation of S6 (Kasimova et al, 2019; Lee and MacKinnon, 2019; Wu et al, 2021; Elbahnsi et al, 2023; Burtscher et al, 2024). HCN channels also display the property of hysteresis, whereby the kinetics of channel closure or deactivation after removal of the hyperpolarizing input is dependent on their previous activation history. This property is thought to be crucial for their role in maintaining rhythmic neuronal firing (e.g., Elinder et al., 2006; Mannikko et al., 2005; Villalba-Galea and Chiem, 2020).

Voltage clamp fluorometry (VCF) (for review, see Cowgill and Chanda, 2019; Priest and Bezanilla, 2015) has played a key role in many of these studies by allowing real-time assaying of localized conformational changes associated with the HCN channel voltage sensor movement (Bruening-Wright et al., 2007; Bruening-Wright and Larsson, 2007; Ramentol et al., 2020; Wu et al., 2021, 2023). In its conventional implementation, as first described by the Isacoff group (Mannuzzu et al., 1996) to probe the *Shaker* K⁺ channel, a cysteine is substituted at a chosen site of interest and covalently labeled with a fluorophore. Changes in the fluorophore's microenvironment down to single amino acid resolution (e.g., Pathak et al., 2007) caused by direct or indirect conformational changes are reported as changes in fluorescence intensity resulting from collisional quenching or other mechanisms. Moreover, analysis of fluorescence time course can provide unique insights into resolving and identifying specific protein conformations induced by substrate and membrane potential (e.g., Patti et al., 2016; Patti and Forster, 2014; Gorraitz et al., 2017; Villalba-Galea et al., 2008). The identification of the local environment near the fluorophore can be further refined by, for example, modifying the quenching conditions (e.g., Cha and Bezanilla, 1998; Papp et al., 2022; Sorensen et al., 2000; Mannuzzu et al., 1996).

Here, we characterize the behavior of two commonly used fluorophores, Alexa Fluor C5-maleimide (ALEXA-488) and 2-((5(6)-Tetramethyl-rhodamine)carboxylamino)ethyl Methanethiosulfonate (MTS-TAMRA) (Fig. 1 A), under the same measurement conditions using excitation and emission hardware appropriate for each label, and present evidence that they report on distinct aspects of HCN voltage-dependent activation. We used the sea urchin sperm HCN channel isoform (spHCN) (Gauss et al., 1998) with an engineered cysteine at position Arg332 at the N-terminal end of the S4 helix (Bruening-Wright et al., 2007) (Fig. 1 B) and expressed in *Xenopus* oocytes. ALEXA-488 labeling at this and other sites has been used extensively to study the role of S4 movement in HCN channel gating (Ramentol et al., 2020; Wu et al., 2021, 2023; Bruening-Wright and Larsson, 2007; Bruening-Wright et al., 2007). In contrast, MTS-TAMRA (and similar rhodamine dyes), which has been used for VCF studies on electrogenic transporters (e.g., Patti et al., 2016; Gorraitz et al., 2017; Loo et al., 2005; Virkki et al., 2006), K_v channels (e.g., Cha and Bezanilla, 1998; Mannuzzu and Isacoff, 2000), and receptors (e.g., Papp et al., 2022; Fryatt and Evans, 2014; Dekel et al., 2012), has so far not been reported as a probe for VCF studies on spHCN channels. In this study, we show that in response to membrane hyperpolarization, ALEXA-488 fluorescence was consistent with a rapid movement of the S4 domain that preceded channel opening in agreement with previous studies (Bruening-Wright et al., 2007; Ramentol et al., 2020; Wu et al., 2021, 2023). In contrast, under the same experimental conditions, the fluorescence emitted by MTS-TAMRA was delayed and correlated with the early phase of channel opening. Both labels also reported a slower component of fluorescence that we show is associated with the mode shift induced by previous hyperpolarization and which depends on the availability of K⁺ ions in the pore. Our findings underscore the need to apply caution when interpreting VCF data and demonstrate that the use of different fluorescent labels may potentially offer new insights into voltage activation of HCN channels.

Materials and methods

Solutions and reagents

Defolliculated oocytes were washed in standard OR-2 solution that contained (in mM) 82.5 NaCl, 2 KCl, 1 $MgCl_2.6H_2O$, and 5 HEPES, adjusted to pH 7.4 with 2-amino-2-(hydroxymethyl)-1,3-propanediol (TRIS). Injected *Xenopus laevis* oocytes were incubated in a standard ND96 storage solution that contained (in mM): 96 NaCl, 2 KCl, 1 $MgCl_2.6H_2O$, 1.8 $CaCl_2.2H_2O$, and 5 HEPES, adjusted to pH 7.4 with TRIS and supplemented with antibiotic gentamicin (50 mg/liter). Electrophysiology was performed using a superfusing solution that contained (in mM) 100 KCl or 100 NaCl, 1.8 $BaCl_2$, 1 $MgCl_2$, and 10 HEPES, pH 7.4 adjusted with TRIS (100K or 100Na solution). Ba^{2+} was substituted for Ca^{2+} to minimize contamination from endogenous Cl^- and K⁺ channel currents. CsCl was added as a powder to the 100K working solution to give a final concentration of 10 mM. For iodide quenching experiments, powdered KI was added to a working solution in which 50% of KCl was replaced with choline chloride to give 50 mM I^- (Patti et al., 2016). The higher osmolarity of this solution was well tolerated by the oocytes. For quenching control experiments (Fig. S3), KI was added from a 1 M stock to give final concentrations of 5, 10, 25, and 50 mM I^-. The total $[K^+]$ was kept constant to mimic the conditions used experimentally with oocytes by replacing KCl in the 100K solution with choline chloride according to the I^- concentration used. Fluorescent labels, ALEXA-488 (Thermo Fisher Scientific), and MTS-TAMRA (mixed isomer) and single isomers (MTS-5-TAMRA, MTS-6-TAMRA) (Biotium) were stored in DMSO at −40°C before use.

cRNA preparation

cDNA encoding the wild type sea urchin (*Strongylocentrotus purpuratus*) HCN channel (spHCN^{WT}) was kindly supplied by Dr. R. Seifert (Max Planck Institute for Neurobiology of Behavior [MPINB], Bonn, Germany), and cDNA for the mutant spHCN-R332C (spHCN^{R332C}) channel was kindly supplied by Prof. H.P. Larsson (University of Linköping, Linköping, Sweden). To improve the protein expression in oocytes, the cDNA was subcloned into the pGEMHE-MCS vector containing the 5′ and 3′ UTRs from *Xenopus* β-globin. The correct DNA sequence was verified by Sanger sequencing. The plasmid was linearized with *Nhe*I-HF (New England Biolabs) and purified using QIAquick PCR Purification Kit (QIAGEN). The quality and concentration of the linearized plasmid were confirmed via gel electrophoresis and Nanodrop Spectrophotometer (Thermo Fisher Scientific). Following, in vitro transcription of cRNA was performed using the linearized cDNA template and the mMessage mMachine T7 transcription kit (Ambion, Thermo Fisher Scientific). For cRNA purification, the RNeasy Mini Kit (QIAGEN) was used. RNA concentration and purity were verified using NanoDrop Spectrophotometer. cRNAs were stored at −80°C.

Expression in *X. laevis* oocytes

Adult female *X. laevis* frogs were anesthetized with 1.3 mg/ml tricaine methanesulfonate (MS-222) and ovaries were surgically removed via a small abdominal incision in accordance with animal handling protocols. Oocytes were defolliculated with 1.5 mg/ml collagenase for 1 h and washed with calcium-free OR-2 solution. Mature oocytes stage V or VI were selected and injected manually with 10 ng of cRNA in a 50-nl injection solution and maintained in ND96 storage solution at 17°C for 2–3 days before use.

Two-electrode voltage clamp (TEVC)

Standard TEVC hardware was used (TEC-05X; NPI. Tamm), with series resistance (R_s) compensation applied to ensure clamp accuracy when oocytes exhibited high functional expression. Micropipettes were filled with 3 M KCl with resistances between 0.2 and 0.5 MΩ. Voltage clamp control and data acquisition were under software control (pClamp version 10; Molecular Devices). All experiments were performed at 18–20°C. Oocytes were placed in a small perfusion chamber (filled volume ∼20 µl) that was continuously perfused by gravity feed via a common manifold and flow was controlled by pinch valves. Solution exchange occurred in typically <4 s (McKenzie et al., 2023). Data were sampled at 50 µs/point and low-pass filtered at 1,000 Hz using the TEC-05X in-built analog Bessel filter.

VCF

The VCF apparatus comprised the TEVC (see above) and a laboratory-built fluorescence microscope mounted below the recording chamber coverslip as previously described (Virkki et al., 2006). For experiments using MTS-TAMRA labeling, oocytes were incubated in the dark at room temperature for ∼15 min in a 100K solution supplemented with 40 µM of the label. For experiments using ALEXA-488, oocytes were incubated for 30–60 min in a 100K solution supplemented with 100 µM of the label. Variation in labeling "efficiency" (comparing activating current amplitude with maximum fluorescence induced by the same voltage step) was observed for oocytes from the same donor frog. The underlying reasons were not further investigated in this study. Following incubation, oocytes were washed in 100K solution and stored in the dark on ice in 100K solution to reduce internalization of labeled channels. For oocytes labeled with ALEXA-488, changes in fluorescence emission were resolved using a XF100-2 cube set (475AF40 excitation filter, 505DRLP dichroic mirror, and 535AF45 emission filter) (Omega Optical Inc.) and excited by a blue LED (L1RX-BLU) (Luxeon, Philips LumiLEDs). For oocytes labeled with MTS-TAMRA, changes in fluorescence emission were resolved using a XF32 cube set (535DF35 excitation filter, 570DRLP dichroic mirror, and 596DF35 emission filter) (Omega Optical Inc.) and excited by a green LED (L1RX-GRN), (Luxeon, Philips LumiLEDs). The LEDs were driven by a stabilized, current source (typically 300–500 mA, depending on the fluorophore), and cell exposure to the light source was controlled by an electronic shutter (VS252T1; Vincent Assoc). After labeling, oocytes were placed animal pole down in the perfusion chamber. The fluorescence signal was detected by a photodiode (S1336-BQ; Hamamatsu) and the diode current was converted to a voltage using an Axopatch 200A (Molecular Devices) amplifier. Diode bias was adjusted to minimize noise and headstage resetting. The output was further amplified, low-pass filtered (8-pole Bessel), and sampled at the same rate as for the TEVC signals. Some photobleaching occurred after multiple light exposures and extended protocols before and after ligand application. Scaling corrections were made based on changes in background fluorescence, where we assumed that all labeled proteins were equally affected. Oocytes expressing spHCN^{WT} channels gave no ΔF in response to voltage steps after incubating with MTS-TAMRA under the same conditions indicated above, as previously reported for ALEXA-488 (Bruening-Wright and Larsson, 2007) (data not shown), which established that labeling of native Cys was unlikely to contribute to ΔF.

Iodide quenching was confirmed using a QE65000 spectrometer (Ocean Optics) coupled to the fluorescence microscope instead of the photodiode (Fig. S3).

Data analysis

Data were analyzed using Prism 9.1 (Graphpad) and Clampfit 10.4 (Molecular Devices). Time constants for activation were obtained from exponential fits using Clampfit routines applied to a region commencing after the initial inflexion to the end of the test pulse. For strong hyperpolarizing potentials, the activation current time course was best described using a double-exponential fit (Hung et al., 2021; Bruening-Wright et al., 2007). The fluorescence signal was described by either a double exponential (MTS-TAMRA labeling) or a variable offset rising exponential (ALEXA-488 labeling) as indicated. All exponential fits used the Chebychev fitting algorithm in Clampfit. The macroscopic conductance (G) was derived from the instantaneous tail currents by assuming a constant driving force and number of channels. First, a baseline correction was made after the current had reached a steady state at +40 mV, and the instantaneous current was measured at the start of the repolarizing step (I_{tail}) immediately after the capacitive transient had settled and fit with a form of the Boltzmann equation:

$$I_{tail} = I_{tail}^{off} + I_{tail}^{max} \bigg/ \left(1 + e^{\frac{\left(V - V_{0.5}^{G}\right) e z^{G}}{kT}}\right) \qquad (1)$$

where I_{tail}^{max} is the maximum instantaneous tail current and I_{tail}^{off} is the offset reported by the fit (typically = 0 with baseline correction), $V_{0.5}^{G}$ is the mid-point voltage, z^{G} the valence of the apparent charge moved, and kT/e = 25.3 mV at 20°C. A similar equation was used to characterize the ΔF–V data with corresponding parameters: midpoint voltage ($V_{0.5}^{F}$) and valence (z^{F}) of the apparent charge moved. Data sets were normalized to the predicted maximum and pooled from replicate data sets. All data points are shown as mean ± SEM and all pooled experimental data were obtained from oocytes from more than two donor frogs unless otherwise noted.

Statistical data analysis was performed using Student's t test or ANOVA as indicated. Data points are presented as mean ± SEM and fitted parameters as mean ± SE.

Kinetic simulations

Kinetic simulations of a 12-state model for HCN channels (Wu et al., 2021) were performed using Berkeley Madonna (v.8.3.9).

Structural modeling

The wild type sea urchin HCN (spHCN$^{\mathrm{WT}}$) (spHCN; UniProtKB entry Q45ZY2) in depolarized and hyperpolarized state conformations were constructed using the SWISS-MODEL server (Waterhouse et al., 2018) with the human HCN1 PDB structures 5U6O and 6UQF (Lee and MacKinnon, 2017, 2019), respectively, as structural templates. Residue Arg332 (spHCN$^{\mathrm{WT}}$; equivalent to Arg258 in HCN1) in both structures was mutated to Cys using Discovery Studio Visualizer (DSV) 2021 (Dassault Systèmes). The structures of free fluorophores ALEXA-488 and MTS-TAMRA were constructed using the small molecule build and geometry optimization modules of DSV. Structures of depolarized and hyperpolarized spHCN$^{\mathrm{R332C}}$ covalently bound to ALEXA-488 or MTS-TAMRA via Cys332 were obtained as follows. First, Autodock Vina 1.1.0 (Eberhardt et al., 2021; Trott and Olson, 2010) was used to predict initial (non-covalent) binding positions of these two fluorophores at spHCN$^{\mathrm{R332C}}$ to identify binding poses that place the ligating atom of these molecules in proximity to Cys332. Single monomers of depolarized and hyperpolarized spHCN$^{\mathrm{R332C}}$ were used for docking calculations, as the sizes of the fluorophores and tethering to Cys332 preclude them from forming multisubunit interactions. The GUI PyRx 0.8 (Dallakyan and Olson, 2015) was used to prepare the Autodock Vina calculations. Blind docking was performed for both fluorophores at both depolarized and hyperpolarized spHCN$^{\mathrm{R332C}}$, with the docking box set to "maximize" in all cases. All rotatable torsions were set to be flexible for the two unligated fluorophores. An exhaustiveness parameter value of 48 was used for all Vina docking calculations. For each fluorophore, we selected the most energetically favored pose in which the molecules are oriented such that their Cys-linking atom was close to Cys332. Second, DSV was used to manually define a covalent bond between Cys332 and the respective fluorophore via a C-S bond for ALEXA-488, and a disulfide (S-S) bond for MTS-TAMRA to produce depolarized and hyperpolarized spHCN$^{\mathrm{R332C}}$ covalently liganded to each fluorophore at position 332. This was followed by energy minimization, using DSV, of the covalently attached fluorophores and residues Val324 to Cys332. This resulted in minor structural corrections for the depolarized spHCN$^{\mathrm{R332C}}$, but partial unwinding of this helical segment for hyperpolarized spHCN$^{\mathrm{R332C}}$, as Cys332 is buried within the extracellular pocket of the VSD (S4) helical bundle in the hyperpolarized state and would require at least local structural disruption to accommodate the fluorophores. Third, the covalent docking protocol implemented in AutodockFR (Bianco et al., 2016) was then used to predict energetically favored positions of ALEXA-488 and MTS-TAMRA while taking into account orientational rigidity imposed by covalent linkage to Cys332. A docking box with a grid spacing of 0.375 Å, centered at Cys332 was defined for both depolarized and hyperpolarized conformations, with dimensions of 20 × 25 × 50 Å^{3} to encompass the entire volume hypothetically accessible to the tethered fluorophores. AutogridFR (Zhang et al., 2019) was used to prepare affinity maps, including intrareceptor gradients. Autodock (Morris et al., 2009) was subsequently performed using 100 independent docking runs, each using up to 10^{5} evaluations, for each fluorophore and spHCN$^{\mathrm{R332C}}$ conformation. The highest-ranked poses for ALEXA-488 and MTS-TAMRA at depolarized and hyperpolarized spHCN$^{\mathrm{R332C}}$ were selected for subsequent analysis. Schrödinger Maestro 12.9 (Release 2021-23; Maestro, Schrödinger) was used to obtain 2-D ligand interaction diagrams for the covalent docking-obtained results.

Online supplemental material

Fig. S1 shows representative current and fluorescence traces for oocytes labeled with MTS-5-TAMRA and MTS-6-TAMRA. Fig. S2 shows mode shift analysis of tail currents from a representative unlabeled oocyte expressing spHCN$^{\mathrm{R332C}}$. Fig. S3 shows a spectroscopic analysis of ALEXA-488 and MTS-TAMRA quenching. Fig. S4 shows the effect of I^{-} on normalized conductance for cells labeled with ALEXA-488 and MTS-TAMRA (Fig. S4 A), and the effect of I^{-} on fast and slow ΔF for ALEXA-488–labeled oocytes (Fig. S4 B). Table S1 shows fit parameters for fitting normalized conductance before and after I^{-} exposure. Table S2 shows fit parameters for fitting ΔF–V data before and after I^{-} exposure. Table S3 shows simulation parameters.

Results

Distinct voltage-dependent fluorescence changes observed after labeling spHCN^{R332C} channels with ALEXA-488 or MTS-TAMRA

We recorded changes in fluorescence (ΔF) from oocytes expressing the spHCN^{R332C} channel that were labeled with either ALEXA-488 (single isomer) or MTS-TAMRA (mixed isomer) (Fig. 1, A and B) in response to hyperpolarizing voltage steps from a 0 mV holding potential. Recordings from two representative oocytes superfused with 100K solution from the same donor frog revealed that the time course of ΔF during channel activation was markedly different for each labeling condition (Fig. 1 C). In response to the voltage step protocol (inset), ALEXA-488–labeled oocytes displayed an initial rapid rise of ΔF, followed by a slower component that reached a steady state by the end of the 1-s test pulse. The rapid rise of ΔF, which was easily resolved for the largest hyperpolarizing steps, was slower than the main component of the capacitive current transient that would account for ∼90% of the membrane charging (see inset, Fig. 1 C). Typically, the 10–90% rise time for the recorded membrane potential was <0.4 ms; however space clamp limitations for the intact oocyte clamp and inhomogeneities in oocyte charging meant that this would not hold for the whole oocyte membrane (e.g., see Baumgartner et al., 1999). Nevertheless, we would expect overall charging to be complete within a few ms of the step onset and therefore would not limit the fast ΔF kinetics observed. The 10–90% rise time of this rapid ΔF component for steps from 0 to −160 mV was 3.95 ± 0.29 ms (n = 6) and was also not limited by the bandwidth of the fluorescence signal conditioning hardware, which had a rise time of 1.75 ms (400 Hz bandwidth). When the membrane potential was stepped back to +40 mV (for instantaneous current tail analysis [see below]), ΔF decayed monotonically and the rapid change in ΔF at step onset was absent when returning from the largest hyperpolarizing test potentials. In contrast, MTS-TAMRA–labeled oocytes displayed a slower increase in ΔF that commenced at completion of the capacitive transient (see inset, Fig. 1 C) and did not reach a steady state during the 1-s hyperpolarizing test pulse. To exclude the possibility that the slower response resulted from the mixed isomer labeling, we performed a control assay by labeling spHCN^{R332C}-expressing oocytes with single isomers. In both cases, ΔF increased with hyperpolarization and a similar delayed response in ΔF following the hyperpolarizing step (see Fig. S1). All subsequent fluorometry using MTS-TAMRA was performed exclusively with the mixed isomer (2-((5(6)-Tetramethylrhodamine)carboxylamino)ethyl Methanethiosulfonate).

The deactivating decay time course for MTS-TAMRA labeling was also monotonic and slower than for ALEXA-488–labeled cells. Moreover, the ΔF deactivation phase for both labeling conditions was also markedly slower than the deactivation phase of the current tails, which indicated that the channel pore closed well before ΔF returned to the baseline. For both current and ΔF, the deactivation time course was well described by a single exponential decay with time constants τ^{I}_{deact} and τ^{F}_{deact}, respectively. For a step from −160 to +40 mV, ALEXA-488 labeling resulted in τ^{I}_{deact} = 15.2 ± 1.3 ms (n = 5) and τ^{F}_{deact} = 87.2 ± 8.8 ms; and MTS-TAMRA labeling resulted in τ^{I}_{deact} = 68.0 ± 6.6 ms (n = 5) and τ^{F}_{deact} = 314.4 ± 48.9 ms. For unlabeled cells expressing spHCN^{R332C}, τ^{I}_{deact} = 24.6 ± 1.8 ms (n = 3). This established that labeling with MTS-TAMRA had slowed the channel closure rate more markedly than ALEXA-488 and confirmed that both fluorophores reported molecular rearrangements involving S4 movement after channels had closed.

Parametric plots at four activation potentials for representative cells indicated that there was no obvious correlation between the overall time course of ΔF_{total} and activating current (I^{act}) for either label (Fig. 1 D). However, for MTS-TAMRA labeling, the initial phase of ΔF (up to 60 ms) tracked the corresponding rapid initial growth of I^{act} (Fig. 1 E), which suggested that this label reported a conformational change that directly related to channel opening. For times >60 ms, after the hyperpolarizing step onset, the parametric plots suggested that ΔF and I^{act} were also tracked for ALEXA-488. Taken together, these findings established that despite being covalently linked to the same cysteine, each label reported different changes to their respective microenvironments as the channels activate and deactivate.

We determined the dependence on the membrane potential of the normalized conductance (G) from instantaneous tail current analysis (see Materials and methods) and compared this with the normalized total fluorescence change (ΔF_{tot}) for each label measured at the end of the test pulse (Fig. 2 A). For both fluorophores, the midpoint voltage of ΔF_{tot} ($V^{F}_{0.5}$) was right shifted relative to that of G ($V^{G}_{0.5}$) by 43 mV (ALEXA-488) and 38 mV (MTS-TAMRA) (Table 1). This indicated that each fluorophore reported conformational changes that preceded channel opening, which was in general agreement with previous findings for spHCN^{R332C} labeled with ALEXA-488 (Bruening-Wright et al., 2007). Labeling oocytes expressing spHCN^{R332C} with either fluorophore also altered the voltage dependence of channel activation: for MTS-TAMRA, when compared with the normalized G-V data obtained from unlabeled oocytes expressing spHCN^{R332C}, $V^{G}_{0.5}$ was right shifted by ∼38 mV, whereas ALEXA-488 labeling resulted in a smaller right shift of 12 mV (Table 1). Thus, labeling with ALEXA-488 influenced the spHCN^{R332C} channel open probability less than MTS-TAMRA, consistent with the altered deactivation rates for current (see above). We found that spHCN^{WT}-expressing oocytes typically showed a −70 mV shift in $V^{G}_{0.5}$ compared with spHCN^{R332C} (Table 1) (see also Mannikko et al., 2002). The larger right shift of $V^{G}_{0.5}$ for MTS-TAMRA suggested that the presence of this label led to a partial compensation for the charge loss that resulted from the removal of Arg332 for spHCN^{WT}.

To characterize activation kinetics further, we compared the activation time course before and after labeling of the time-dependent (activating) component of membrane current and fluorescence following the voltage step onset (Fig. 2 B). For unlabeled and labeled oocytes, current activation was well described by fitting a double exponential function commencing after the capacitive transient had settled, in agreement with previous studies (Bruening-Wright et al., 2007). We only considered time constants reported by the double exponential fit for potentials less than or equal to −60 mV, where an obvious time-dependent activation was observed. For unlabeled and labeled

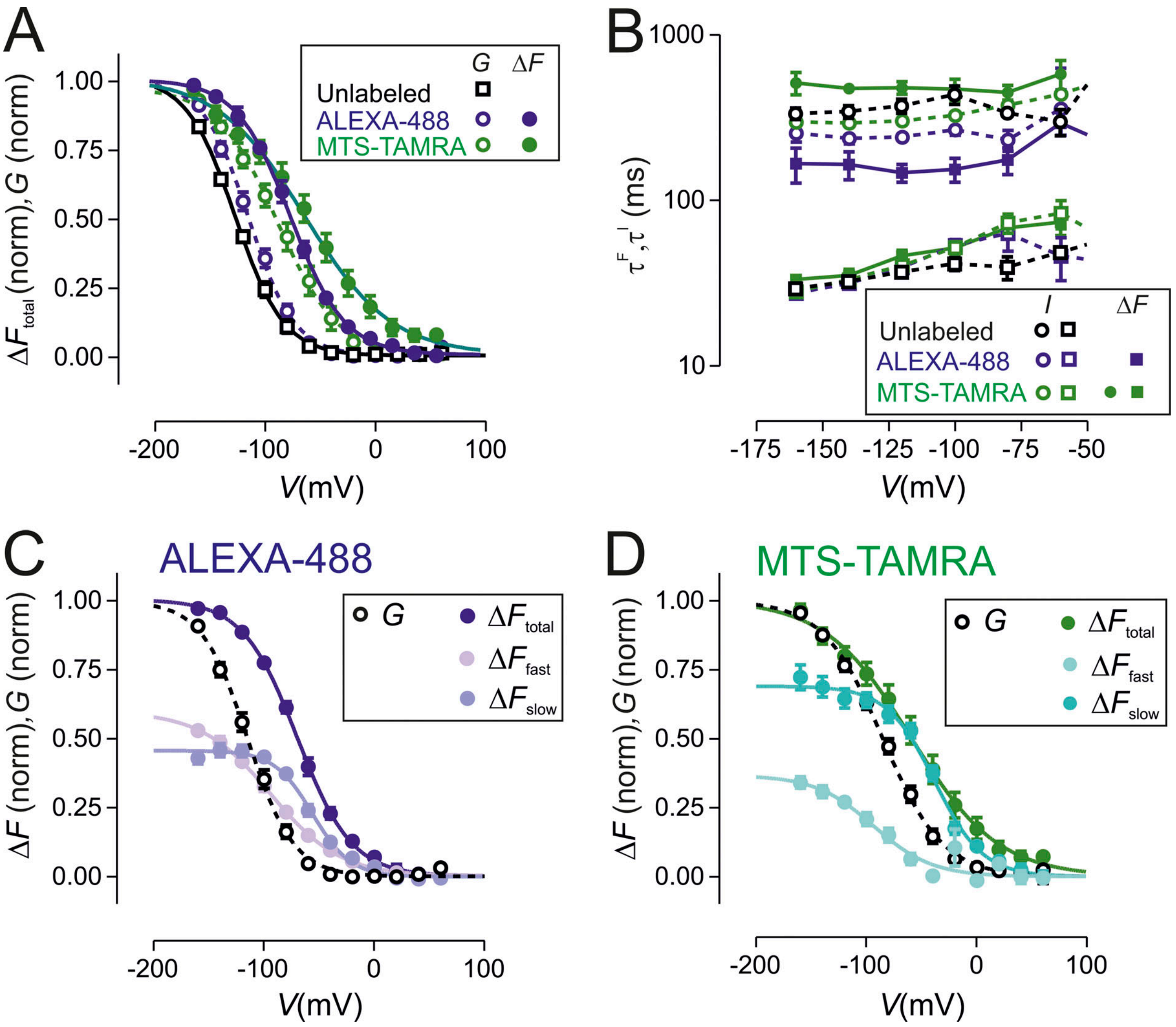

Figure 2. **Comparison of voltage-dependent properties of unlabeled and labeled spHCN^{R332C}. (A)** Conductance (G) derived from tail currents and total ΔF (ΔF_{total}) measured at the end of 1-s test pulse normalized to respective maxima predicted from Boltzmann fit to data sets from individual oocytes and then pooled (see Materials and methods). Open symbols: G; filled symbols, ΔF_{total}. Unlabeled spHCN^{R332C}: n = 3; ALEXA-488–labeled spHCN^{R332C}: n = 5; MTS-TAMRA labeled; n = 5. Symbols shown in boxed inset. **(B)** Activation time constants plotted as a function of test pulse for current (τ^{I}) and ΔF (τ^{F}) compared for labeled and unlabeled cells. For both labels, activation currents were fit with two exponential: for ALEXA-488–labeled oocytes, ΔF was fit with a single rising exponential with variable offset for ALEXA-488 labeling and a double exponential for MTS-TAMRA labeling. ALEXA-488–labeled spHCN^{R332C}: n = 15; MTS-TAMRA–labeled spHCN^{R332C}: n = 9; unlabeled spHCN^{R332C}: n = 6. Symbols shown in boxed inset. A one-way ANOVA test reported no significant difference ($P < 0.05$) between the means of the fast component of τ^{I} for the unlabeled and each labeled case in the potential range −160 to −80 mV. There was no significant difference (t test, $P < 0.05$) between the means in the potential range −160 to −80 mV when comparing the fast components of τ^{I} and τ^{F} for TAMRA labeling reported. **(C)** For ALEXA-488–labeled oocytes, ΔF_{total} was resolved into two components (ΔF_{fast}, ΔF_{slow}) when fit with a single rising exponential with variable offset, where ΔF_{fast} represents the fit offset and ΔF_{slow} represents the amplitude of the exponential component. Same data set as in B. Data shown normalized to ΔF_{total}. Symbols shown in boxed inset. **(D)** For MTS-TAMRA–labeled oocytes, $\Delta F_{total}$was resolved into two components (ΔF_{fast}, ΔF_{slow}) when fit with a double exponential function. Same data set as in B. Data shown normalized to ΔF_{total}. Symbols shown in boxed inset.

oocytes, the faster time constant showed a similar voltage dependence for potentials less than or equal to −100 mV with no statistical difference (see legend, Fig. 2 B), whereas the slower components showed a weak voltage dependence over the same voltage range. For ALEXA-488–labeled oocytes, fitting the complete ΔF traces with a standard double exponential function resulted in large fit uncertainty at the step onset and we therefore chose to describe ΔF by a single rising exponential with variable offset (see Materials and methods). This allowed us to separate ΔF_{total} into two components: an initial pseudo instantaneous change (ΔF_{fast}) and a slower time-dependent component (ΔF_{slow}) described by a single exponential rise to the steady state. The time constant for ΔF_{slow} showed little voltage dependence up to −60 mV, and it was significantly slower than the main fast time constant for current activation (Fig. 2 B). Both components of fluorescence showed different steady-state voltage dependencies (Fig. 2 C) with midpoint voltages lying to the right of the corresponding conductance midpoint ($V^{G}_{0.5}$) (Table 1). This indicated that each component reflected unique molecular conformational changes involving

Table 1. **Comparison of Boltzmann fit parameters from normalized conductance (G) or change in fluorescence (ΔF) for spHCN^{WT}, spHCN^{R332C} in 100K solution**

	Parameter	**spHCN^{WT} (5)**	**spHCN^{R332C}**		
			Unlabeled (3)	**ALEXA-488 (5)**	**MTS-TAMRA (8)**
G	$V_{0.5}{}^{G}$ (mV)	−56.1 ± 2.4	−126.9 ± 2.4	−114.6 ± 2.4^{a}	−88.7 ± 3.9^{a}
	z^{G}	1.30 ± 0.12	1.17 ± 0.13	1.24 ± 0.09^{a}	0.94 ± 0.09^{a}
ΔF	ΔF_{total}			**ALEXA-488 (14)**	**MTS-TAMRA (7)**
	$V_{0.5}{}^{F}$ (mV)			−71.9 ± 1.7^{a}	−59.0 ± 6.0^{a}
	z^{F}			1.05 ± 0.06^{a}	0.66 ± 0.07^{a}
	ΔF_{fast}				
	$V_{0.5}{}^{F}$ (mV)			−96.4 ± 2.0	−93.5 ± 12.2
	z^{F}			0.77 ± 0.04	0.97 ± 0.29
	ΔF_{slow}				
	$V_{0.5}{}^{F}$ (mV)			−53.3 ± 2.10^{a}	−38.0 ± 2.10^{a}
	z^{F}			1.51 ± 0.16	1.19 ± 0.01

Values are shown as mean ± SE as reported by fit to normalized pooled data using the Boltzmann equation (Eq. 1). Number of cells analyzed given in parentheses. ΔF_{total}measured at end of 1-s test pulse at each potential for both labels. $\Delta F_{fast,slow}$ refer to components obtained by fitting a single exponential plus offset to ALEX-488 data or double exponential to MTS-TAMRA data (see text).

[a]Indicates significant difference between ALEXA and MTS-TAMRA fit parameters (t test, $P < 0.05$).

S4 that preceded channel opening. Component ΔF_{slow} was resolved at potentials well before most channels would be open and increased in relative amplitude to reach a maximum close to $V_{0.5}^{G}$ before slightly decreasing at the largest hyperpolarizing potentials. Component ΔF_{fast} showed a sigmoidal dependence on V that, together with its absence at the "OFF" transition (see above), would argue against it arising from an electrochromic effect (see Discussion). The similarity of its midpoint voltage (−96 mV) with that reported for gating charges recorded from spHCN^{R332C} channels (−91 mV, see Bruening-Wright et al., 2007) strongly suggested that this component reflected changes in the fluorophore's microenvironment as the charged S4 domain of the VSD moved inward in response to membrane hyperpolarization (Wu et al., 2021).

The ΔF traces for MTS-TAMRA labeling were described by a standard double exponential fit as for the activating current. The time constants associated with each component were generally well separated (greater than fivefold) although resolution of two time constants was difficult for membrane potentials greater than −60 mV due to limited signal-to-noise ratio (Fig. 1 A, right panel). The time constant of the slow component showed no systematic voltage dependence for $-160 \text{ mV} \leq V \leq -60 \text{ mV}$ (Fig. 2 B). To decrease the fit uncertainty, we reduced the number of fit parameters by constraining the slow time constant to the mean of the free fit estimates for voltages from −160 to −80 mV for individual oocytes. The fast time constant was similar in voltage dependence and magnitude to the fast component of the activating current and showed no statistical difference for test potentials less than or equal to −80 mV (see legend, Fig. 2 B). The voltage dependence of the predicted steady-state fluorescence associated with each component (ΔF_{fast}, ΔF_{slow}) was markedly different (Fig. 2 D). For small hyperpolarizations, ΔF_{slow} accounted for most of the total fluorescence and its midpoint potential (approximately −38 mV) obtained from a Boltzmann fit was significantly right shifted relative to that of the corresponding G for MTS-TAMRA–labeled spHCN^{R332C} channels, whereas ΔF_{fast} had a midpoint voltage comparable with $V_{0.5}^{G}$ (Table 1). Together with the similarity of the fast time constants for current and fluorescence at extreme hyperpolarizing potentials (Fig. 2 B), this behavior suggested that ΔF_{fast}reported conformational changes associated with channel opening and was consistent with the early phase of activation depicted in the parametric plot (Fig. 1 C).

In summary, the ALEXA-488 ΔF was consistent with it reporting the initial activation steps involving independent movement of the VSDs, whereas MTS-TAMRA reported on conformational changes associated with channel opening. In addition, both labels reported a second fluorescence component with slower kinetics that did not correlate with channel opening. The most likely functional correlate for this component would be the mode shift or hysteresis, whereby the voltage dependence of activation depends on the previous history of the channel (Bruening-Wright and Larsson, 2007; Elinder et al., 2006; Mannikko et al., 2005) as investigated below.

ALEXA-488 and MTS-TAMRA bound to the S4 domain appear to report on different aspects of HCN channel gating

To further characterize the origins of ΔF, we reduced the test pulse period to 8 ms so that fewer channels would have time to transition to the open state during hyperpolarization. We chose 8 ms as the shortest pulse period that would allow ΔF to be resolved reliably and ensure completion of the capacitive transient using the whole oocyte voltage clamp. In addition, signal averaging (typically from four or eight trials) was employed to improve the ΔF signal-to-noise ratio. If $\Delta F_{fast}$for ALEXA-488 labeling were associated with the initial independent VSD movement, we would expect to see this component return rapidly to the baseline fluorescence upon deactivation. Data from a representative ALEXA-488–labeled oocyte (Fig. 3 A, left panel) showed the characteristic rapid increase in Δ*F* in response to the hyperpolarization. This was followed by a corresponding rapid decrease in direct response to the voltage step returning to +40 mV, together with a slowly relaxing component that diminished in amplitude with weaker hyperpolarizing potentials. In contrast, for a representative MTS-TAMRA–labeled oocyte recorded under the same conditions (Fig. 3 A, right panel), resolvable Δ*F* was only observed for strong hyperpolarizing test pulses. This would be expected if MTS-TAMRA fluorescence reported conformational changes associated with channel opening given that most channels remained closed during the test pulse.

For ALEXA-488 labeling, we measured the peak Δ*F* reached at the end of the test pulse. This showed a sigmoidal voltage dependence (Fig. 3 B) and a Boltzmann fit reported a midpoint voltage ($V^F_{0.5}$) of −107.8 ± 5.0 mV and z^F = 0.73 ± 0.05 (*n* = 9). These fit parameters were in agreement with those obtained by fitting ΔF_{fast} using the longer 1-s pulse activation protocol (Table 1) and further supported the notion that this component of Δ*F* reflected the rapid movement of the VSDs. Moreover, a single exponential fit to the rising phase of Δ*F* showed a "bell-shaped" voltage dependence (Fig. 3 C) with a peak close to $V^F_{0.5}$. A free fit to the time constant using a two-state model (Fig. 3 C legend) gave a similar estimate for z^F (0.82 ± 0.15) (Fig. 3 B).

To further characterize Δ*F* for each labeling condition, we used a variable pulse width protocol with 8-ms increments stepping to −160 mV to fully activate channels (Fig. 3 D). With increasing pulse width, the rapid component of deactivation reported by ALEXA-488 decreased and the amplitude of the slow component of Δ*F* during the deactivating phase grew (Fig. 3 D, left panel). This behavior was consistent with the notion that the activation and deactivation pathways comprise distinct kinetic processes. For the MTS-TAMRA–labeled oocyte, Δ*F* appeared to track the early growth in the activating component of I_m with increasing pulse width (Fig. 3 D, right panel), thereby further supporting the previous observation (Fig. 1 C) that MTS-TAMRA reported conformational changes associated with channel opening, in contrast to ALEXA-488, for which neither component appeared to correlate.

Further insight into identifying the possible functional correlates of the fluorescent responses was obtained using the 12-state allosteric model proposed recently (Wu et al., 2021) (Fig. 4 A, see SI for simulation details). As originally proposed, Δ*F* for the ALEXA-488–labeled case comprises two components corresponding to the independent and concerted S4 movements, respectively. In contrast to Wu and colleagues, we assigned a positive intrinsic Δ*F* to both these components to account for our experimental findings. The simulated ΔF_{total} recapitulated the basic behavior that we observed experimentally if we assumed that ALEXA-488 reports both movements, whereas MTS-TAMRA only reports on the slow movement. According to the model, for strong hyperpolarizing potentials, after the initial rise in fluorescence, the rapid component (ΔF_1) decreased as more S4 subunits undergo the concerted movement and channels open (Fig. 4 B). There was a complementary rise in the Δ*F* corresponding to this concerted step (ΔF_2) so that ΔF_{total} was nearly constant for most of the activation period. Our simulations also indicated that there was a close match between the voltage dependence of conductance (*G*) and ΔF_2 as observed experimentally (Fig. 2 D and Table 1), whereas ΔF_{total} preceded the channel opening (Fig. 4 C). Our simulations were also able to recapitulate the variable pulse protocol findings (compare Fig. 3 D with Fig. 4 D). However, this model was unable to account for the slower component of Δ*F* observed for both fluorophores, which we now show is related to the mode shift behavior as previously reported (Bruening-Wright and Larsson, 2007).

ALEXA-488 and MTS-TAMRA report development of mode shift in spHCN^{R332C} channels

A previous study of spHCN using fluorescent labeling with ALEXA-488 at sites in S4 other than 332, lying at the N-terminal end of S4, reported a strong correlation between the respective time course of Δ*F* and the temporal development of mode shift (as evidenced by the tail current delay). This observation established that the S4 domain undergoes conformational changes during the mode shift (Bruening-Wright and Larsson, 2007). Moreover, in two earlier studies, the mode shift kinetics for mammalian HCN channels were shown to be strongly associated with the presence of external K$^+$ ions in the conductance pathway and their ability to access a binding site within the pore (Mannikko et al., 2005; Elinder et al., 2006). We re-examined these findings in the context of identifying the slow component of Δ*F* observed for each label under our measurement conditions.

We first investigated the effect on Δ*F* of changing the main permeant cations for both labels. The addition of 10 mM CsCl to the standard 100K superfusate (100K+Cs solution), resulted in a block of inward activating current and ΔF^{max}_{total} increased by ∼20% (ALEXA-488) and ∼30% (MTS-TAMRA) (Fig. 5 A, left [ALEXA-488] and right [MTS-TAMRA] panels, Table 2) but only for hyperpolarizing potentials below −60 mV. Substitution of most of the external K$^+$ ions with Na$^+$ ions (100Na solution containing 2 mM KCl) reduced the activating current as expected for a permeability ratio (P_{Na}/P_K = 0.18) (Gauss et al., 1998; Ludwig et al., 1998) (see insets, Fig. 5 B). Superfusion with 100K+Cs solution also resulted in increased ΔF^{max}_{total} of 10% for ALEXA-488 and 30% for MTS-TAMRA (Fig. 5 B, left [ALEXA-488] and right [MTS-TAMRA], Table 2). The increase in ΔF_{total} occurred at potentials less than −60 mV for both fluorophores, which suggested that they most likely report on the same molecular rearrangements induced by the experimental manipulations that altered the availability of K$^+$ ions in the pore (Bruening-Wright and Larsson, 2007). For ALEXA-488 labeling, we also found for both solution manipulations that ΔF_{fast} remained essentially unchanged (Fig. 5, C and D, upper panels) with no significant shift in $V_{0.5}{}^F$ and z^F (Table 2). This established that the rapid S4 movement reported by ALEXA-488 was insensitive to these altered pore permeation conditions or complete block. On the other hand, ΔF_{slow} increased in both cases for potentials below −60 mV, peaked at −100 mV, and then decreased at the strongest hyperpolarizing potentials (Fig. 5, C and D, lower panels),

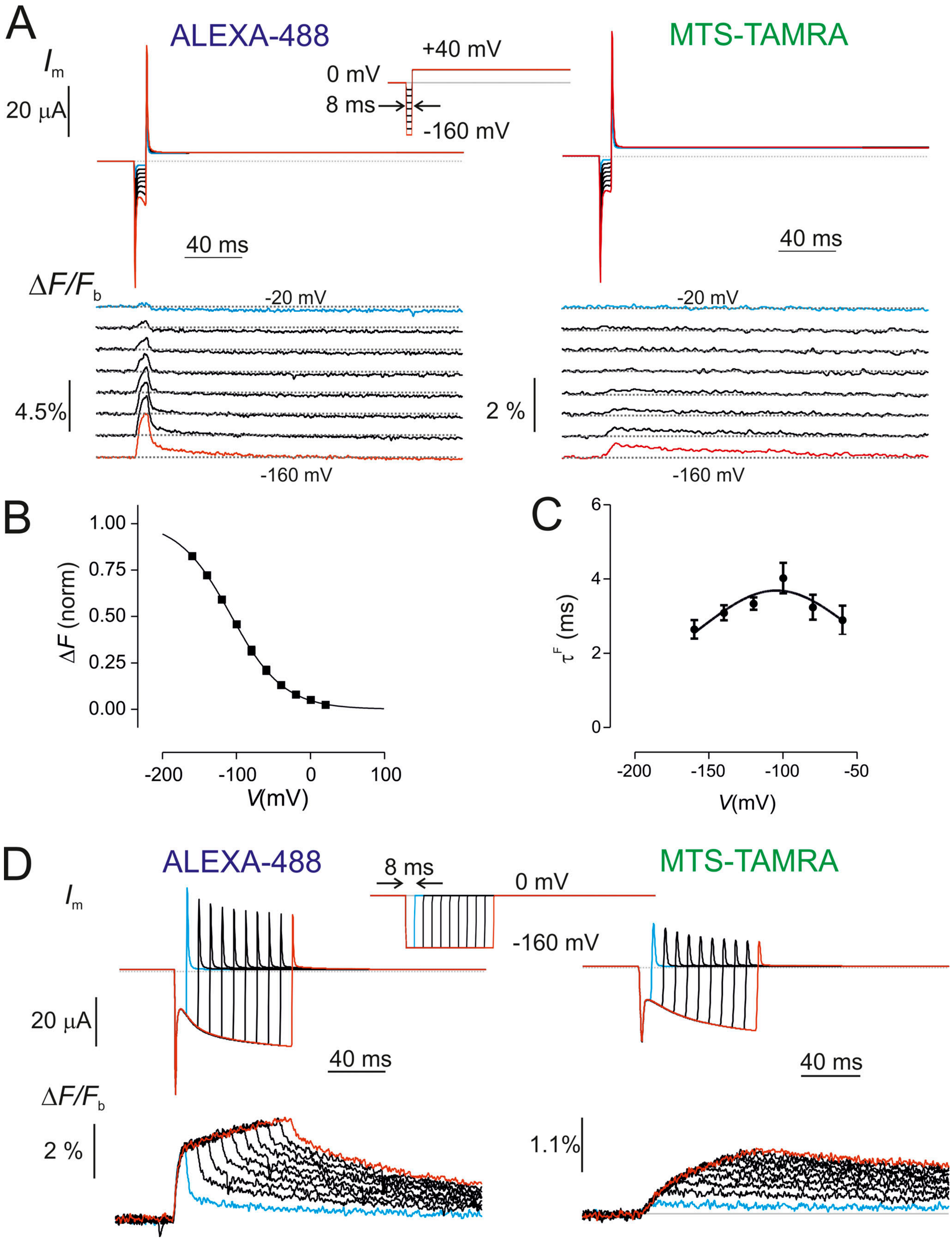

Figure 3. **Voltage step protocols highlight different fluorescent responses for each label. (A)** Representative current and Δ*F* recordings for ALEXA-488 (left) and MTS-TAMRA (right) labeled oocytes using an 8-ms voltage step (inset) showing current (upper) and fluorescence (below). The traces were signal

averaged eightfold to improve the signal-to-noise ratio and separated vertically for visualization. Δ*F* shown as a percentage of background fluorescence. **(B)** Δ*F*-*V* for ALEXA-488–labeled cells. The peak Δ*F* at each voltage at the end of the 8 ms step was first fit with the Boltzmann function and normalized for each cell to ΔF^{max} before pooling. Continuous curve is Boltzmann fit with $V_{0.5}{}^{F}$ = −107.8 ± 5.0 mV; z^{F} = 0.73 ± 0.05; mean ± SE (*n* = 9). **(C)** Voltage dependence of time course for rising phase of Δ*F* for ALEXA-488–labeled cells (same data set as in B) obtained by fitting with a single exponential. It was not possible to resolve reliable fits for voltages above −60 mV. The continuous line is a free fit with a two-state model equation (assuming a symmetrical energy barrier) $(\tau^{F} = 1/\left(k_f e^{-\frac{V}{2kT}ez^{F}} + k_b e^{+\frac{V}{2kT}ez^{F}}\right)$, where $k_{f,b}$ are the forward and backward rates, respectively, and z^{F} is the apparent valence. The fit yielded the following parameters: z^{F} = 0.82 ± 0.15; k_f = 0.024 ± 0.009 and k_b = 0.76 ± 0.24; mean ± SE (*n* = 9). **(D)** Representative current and Δ*F* recordings for ALEXA-488 (left) and MTS-TAMRA (right) labeled oocytes in response to a sequence of prepulses to −160 mV with increasing length (inset) showing current (upper) and fluorescence (below). The traces were signal averaged eightfold to improve the signal-to-noise ratio. Δ*F* shown as a % of background fluorescence.

---

reminiscent of the negative Δ*F* component recently reported under comparable superfusion conditions (Wu et al., 2021).

To examine if the mode shift was reflected in Δ*F*, we used the prepulse protocol incrementing in 8 or 80 ms intervals with a deactivating step to +40 mV and assessed the behavior of tail currents and Δ*F* under three superfusion conditions as above. Fig. 6, A and C, show representative data sets for ALEXA-488 and MTS-TAMRA labeling, respectively, with 80-ms prepulse increments. For both labeling conditions, superfusion with 10 mM CsCl added to the external medium (100K+Cs) blocked the activating current and increased total Δ*F*. Moreover, the normalized tail currents relaxed with a longer delay (quantified as the time to half amplitude; $t_{0.5}^{tail}$) (see Bruening-Wright and Larsson, 2007) relative to the tail current delay at 80 ms (Fig. 6, B and D). When superfused with 100Na solution containing only 2 mM KCl, Δ*F* increased as for superfusion with 100K+Cs and $t_{0.5}^{tail}$ was further delayed. We excluded tail data that was obviously contaminated by endogenous currents activated during longer prepulses, which most likely accounted for the greater variability between individual cells (see Discussion). Qualitatively similar results were obtained with an unlabeled spHCN^{R332C} (Fig. S2), which confirmed that the dependence of $t_{0.5}^{tail}$ on external superfusate was not an indirect effect of the labeling.

Fig. 6, E and F, compare the time course of development of normalized I^{act} and Δ*F* with $t_{0.5}^{tail}$ at −160 mV for prepulse widths up to 488 ms overlaid on the I^{act} and Δ*F* data for each fluorophore. With ALEXA-488 labeling, there was no correlation between I^{act} and Δ*F* for 100K superfusion in agreement with our previous finding (Fig. 1 D); however, Δ*F* tracked the time course of $t_{0.5}^{tail}$ over the whole range examined. This supported the notion that under these conditions the slow component of ALEXA-488 fluorescence reported conformational changes associated with the development of the mode shift. However, for 100K+Cs and 100Na superfusion, $t_{0.5}^{tail}$ only tracked Δ*F* for prepulse periods up to 100 ms (Fig. 6 E, insets), which indicated that under conditions of low availability of K^+ ions in the pore, the slow component of ALEXA-488 also reported conformational changes associated with pore opening. For MTS-TAMRA labeling, I^{act} and Δ*F* correlated for prepulse periods <88 ms (Fig. 6 F, inset) as expected from the parametric plots (Fig. 1, D and E), and $t_{0.5}^{tail}$ for prepulse periods >88 ms tracked the time course of Δ*F*, consistent with MTS-TAMRA reporting both channel opening and mode shift conformational changes. For 100K+Cs superfusion, Δ*F* and $t_{0.5}^{tail}$ deviated in the early phase, whereas for 100Na superfusion Δ*F* and $t_{0.5}^{tail}$ tracked over the whole of the time window investigated.

In summary, these findings provide new evidence that spHCN channels display mode shift in their deactivation kinetics that depends on the availability of K^+ ions in the pore. The development of tail current delay with increasing hyperpolarization period at −160 mV can account for part of the Δ*F* reported by both labels at Cys332 during the channel activation phase.

Quenching experiments and structural modeling suggest that the fluorophores report environments with different solvent accessibility during activation

To gain further insight into the underlying reasons for the different characteristics of each fluorophore, we explored the effect of superfusion with the collisional quencher, iodide. Externally applied iodide should only cause fluorescent quenching of reactive sites if they are accessible to the external solution (Patti et al., 2016; Cha and Bezanilla, 1998; Mannuzzu et al., 1996). We confirmed that both fluorophores in solution were quenched similarly and showed a reasonably linear Stern–Volmer plot expected for a collisional quencher and with comparable slopes (see Fig. S3). Addition of 50 mM I^- to the bath solution resulted in a reduction in background fluorescence by ∼10% and 20% for ALEXA-488–labeled oocytes (*n* = 9) (Fig. 7 A) and MTS-TAMRA–labeled oocytes (*n* = 8) (Fig. 7 C), respectively. Exposure to I^- had only a marginal effect on the steady state open probability of the labeled channels and ∼10% increase in maximum conductance at −160 mV for both fluorophores (Fig. S4). For these experiments, K^+ remained constant (100 mM), and we attributed this effect to changes of anion composition in the pore, which is known to alter the conductance of HCN channels (Wahl-Schott et al., 2005). For ALEXA-488–labeled oocytes, the predicted maximum total fluorescence (ΔF_{total}^{max}) at extreme hyperpolarizing potentials was reduced by ∼25%; however, Δ*F* showed negligible change in $V_{0.5}{}^{F}$ or apparent valence (z^{F}) as reported by a Boltzmann fit to the Δ*F*–*V* data (Fig. 7 B and Table 3). Moreover, in the presence of I^-, both components of Δ*F* were reduced similarly without significant change in the midpoint voltage or apparent valence (Fig. S4 B). In contrast, for MTS-TAMRA–labeled oocytes, a Boltzmann fit to ΔF_{total} reported only a small reduction in ΔF_{total}^{max} accompanied by a 15 mV left shift in $V_{0.5}{}^{F}$ and reduced z^{F} (Fig. 7 D and Table 3). These findings indicated that during channel activation, each fluorophore experienced a different I^--accessible environment as a consequence of voltage-induced conformational changes: for ALEXA-488–labeled oocytes, the reduction in ΔF_{total} over the whole voltage range examined was consistent with this label remaining in a solvent-accessible environment independent of its position, as it moved in response to S4 movement. In contrast, for MTS-TAMRA labeling, the fluorophore was less affected by I^- exposure,

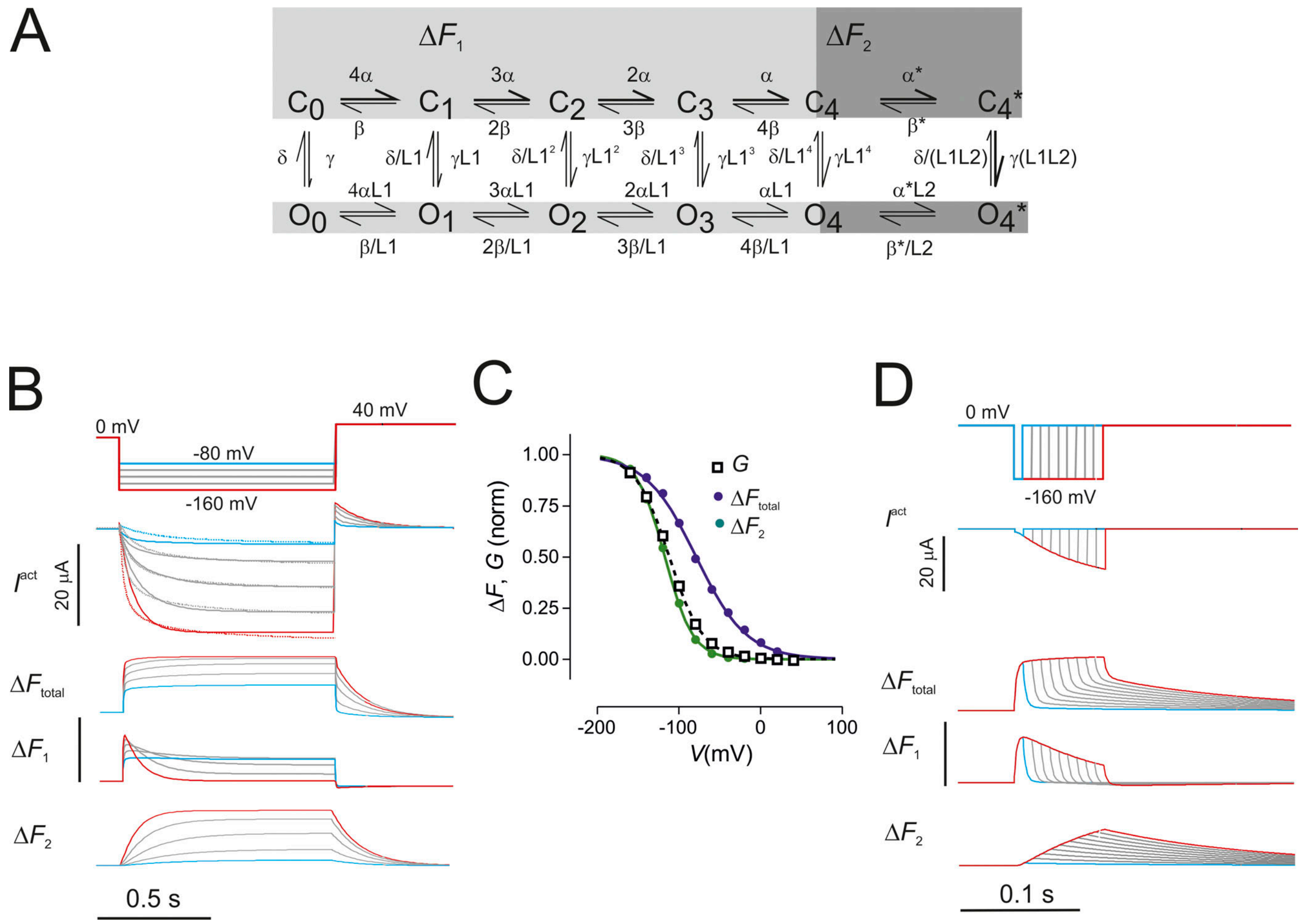

Figure 4. **Simulations using an allosteric 12-state model recapitulate features ΔF obtained with ALEXA-488 and MTS-TAMRA. (A)** HCN allosteric model based on the scheme originally proposed by Altomare et al. (2001) and extended to 12 states (Wu et al., 2021) was used to simulate activating current and fluorescence using their labeling convention. This scheme does not take account of hysteresis (mode-shift), which would require a more complex model with concomitantly more parameters (e.g., see Männikkö et al., 2005). Vertical transitions represent the closed-to-open transition of the pore and were assumed electroneutral. Horizontal transitions between states $C_{0..4}$ and $O_{0..4}$ are voltage-dependent and involve independent movement of S4 helices. If all S4 helices have completed their fast transition, a second concerted movement of S4 helices (transitions C_4-C_4^*, O_4-O_4^*) is proposed to occur. The forward and backward rates of all voltage-dependent transitions were described using the conventional Eyring transition state formulation given by: $\alpha = \alpha_{0,j}e^{-Vz_je/kT}$, $\beta = \beta_{0,j}e^{Vz_je/kT}$, respectively, where e, k, and T have their usual meanings and z_j is the apparent valence for the transition. Zero voltage rates α_0,β_0 were defined as $\alpha_{0,j} = k_je^{\frac{z_je}{kT}V_{0.5,j}}$ and $\beta_{0,j} = k_je^{\frac{-z_je}{kT}V_{0.5,j}}$, where j refers to the fast or slow movement. **(B)** Simulations of I^{act}, ΔF in response to voltage step protocol (top). For simulating I^{act}, we determined a set of model parameters (Table S1) based on a fit to the representative data set of measured activating currents with ALEXA-488 labeling that gave a reasonable match to our data. To simulate the fluorescence in response to voltage steps, we assumed that each of the 12 conformational states can contribute to ΔF_{total}, i.e., $\Delta F_{total} = \sum_{i=0}^{12}\delta_i^F X_i$, where X_i is the state occupancy and δ_i^F is the apparent fluorescence intensity for state i. We assumed that the independent S4 movements (for either open or closed pore) contribute the same fluorescence change per sensor, δ_1^F, $\Delta F_1 = \sum_{i=1}^{4} i\delta_1^F(C_i + O_i)$), whereas the concerted slow movement contributes a change in fluorescence $\Delta F_2 = 4(C_4^*+O_4^*)\delta_2^F$. To account for the difference in ΔF_{total} found experimentally for ALEXA-488 and MTS-TAMRA labeling, we assumed the former reported both fast and slow S4 movements, whereas the latter only reported the slow component. We did not take account of the differences in activation kinetics for the two labels. **(C)** The voltage dependence of normalized conductance (G) and ΔF contributions. ΔF_{total} would correspond to the fluorescence measured by ALEXA-488, whereas ΔF_2 would correspond to that from MTS-TAMRA labeling. Note that the voltage dependence of normalized G and ΔF_2 match well. The fit parameters reported by a single Boltzmann fit were as follows: for G, $V_{0.5}$ = −111.7 ± 0.5 mV, z = 1.26 ± 0.02; for ΔF_{total}, $V_{0.5}$ = −78.9 ± 2.2 mV, z = 0.84 ± 0.06; for ΔF_2, $V_{0.5}$ = −117.1 ± 0.06, z = 1.51 ± 0.04 (mean ± SE). **(D)** Simulations of variable prepulse width protocol with an 8-ms increment (compare with Fig. 3 D). As in B, ΔF_{total} is proposed to represent the ALEXA-488–labeling case, whereas ΔF_2 would represent the MTS-TAMRA–labeling case.

particularly at extreme hyperpolarizations, which suggested that it remained in a largely solvent-inaccessible position.

To examine if these experimental findings had any structural correlates, we predicted binding poses for each fluorophore covalently bound to Cys332 for the closed (depolarized) and open (hyperpolarized) structures as shown in Fig. 8. For MTS-TAMRA labeling, under both depolarizing (Fig. 8 A, left panel) and hyperpolarizing (Fig. 8 A, right panel) conditions, the fluorophore adopted a "downward" facing orientation, which placed the bulk of the molecule deep within the bilayer core.

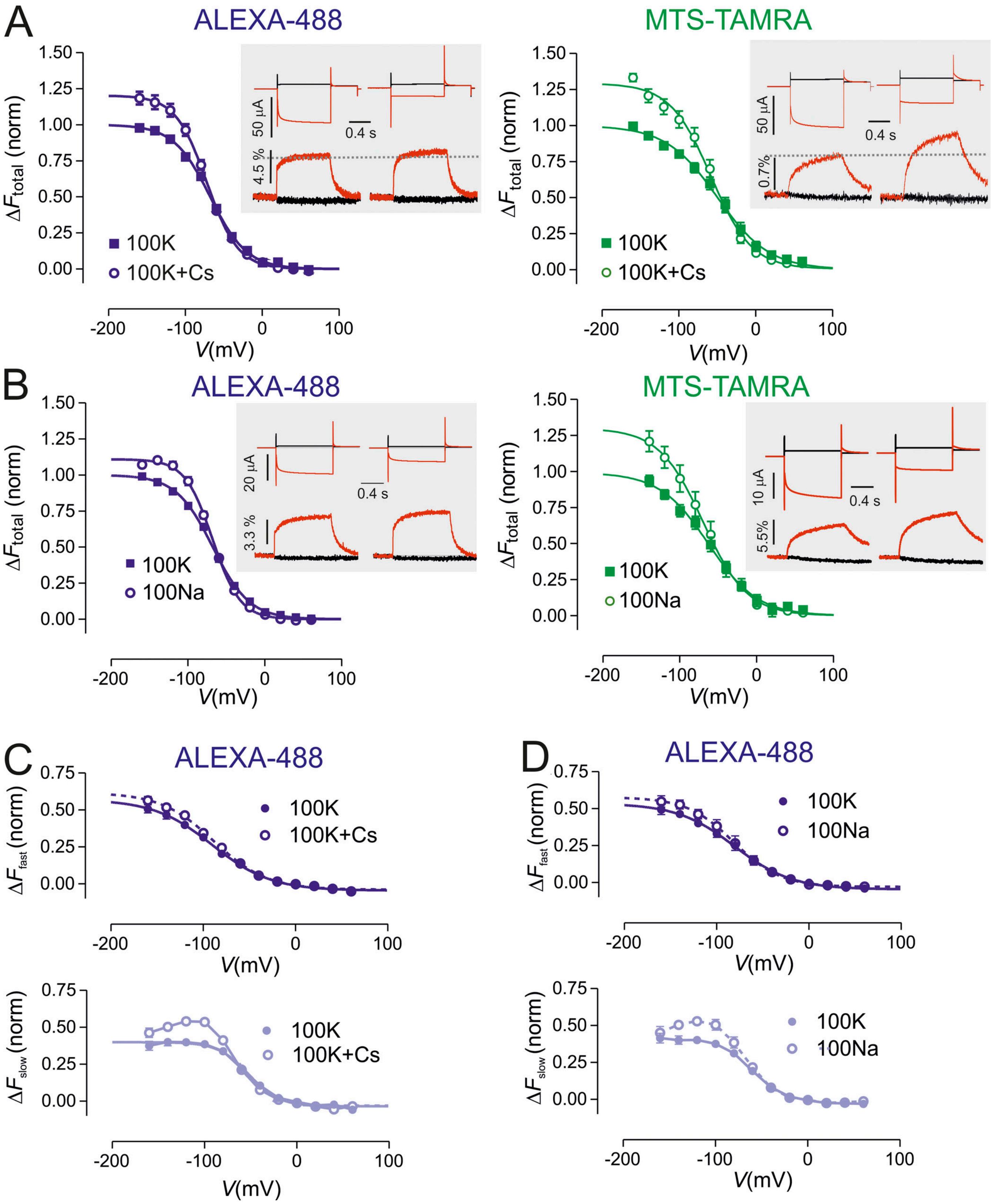

Figure 5. **ΔF for both labels increases after changing permeation conditions. (A)** ΔF–V data before and after addition of 10 mM CsCl to a bath containing standard 100K solution for spHCN^{R332C} expressing oocytes labeled with ALEXA-488 (left panel) and MTS-TAMRA (right panel). Insets show representative membrane current (upper traces) and ΔF (lower traces) for voltage steps to −160 and +20 mV from 0 mV holding potential and ΔF shown as % of background fluorescence. In both cases, the total ΔF was measured at the end of the test pulse. ΔF–V data were fit with the Boltzmann equation (Eq. 1) (continuous lines). Parameters given in Table 2. ΔF–V data were normalized to control condition (100K superfusion) for n = 9 replicates. **(B)** ΔF–V data before and after replacing

bath solution with 100Na solution to give 2 mM KCl for spHCN^{R332C} expressing oocytes labeled with ALEXA-488 (left panel) and MTS-TAMRA (right panel). Insets show representative membrane current (upper traces) and ΔF (lower traces) for voltage steps to −160 and +20 mV from 0 mV holding potential and ΔF is shown as percentage of background fluorescence. Data analysis as in A for n = 5 replicates. **(C)** ΔF–V data for ALEXA-488 labeling showing fast (upper panel) and slow (lower panel) components before and after addition of 10 mM CsCl to the bath as in A. Data were analyzed by fitting ΔF_{total} with a single exponential plus variable offset (see Materials and methods) and normalized with respect to ΔF_{total}^{max}. A t test performed on the fit parameters ΔF_{fast} (Table 2) showed no significant difference between the 100K and 100K+Cs parameters ($P < 0.05$). **(D)** ΔF–V data for ALEXA-488 labeling showing fast and slow components before and after replacement of 100K with 100Na solution to give 2 mM KCl as in B. Data were analyzed by fitting ΔF_{total} with a single exponential plus variable offset (see Materials and methods) and normalized with respect to ΔF_{total}^{max}. A t test performed on the fit parameters ΔF_{fast} (Table 2) showed no significant difference between the 100K and 100Na parameters ($P < 0.05$).

Although the immediate environment remained similar under both conformations, the identities of residues surrounding the fluorophore changed markedly (Fig. 8 A, insets). In the depolarized (closed) state, 2-D ligand interaction diagrams predicted that the rhodamine head group of MTS-TAMRA responsible for fluorescence is surrounded by hydrophobic residues of S5 and S6. During hyperpolarization, the pattern of surrounding residues changes to less polar ones, thereby explaining reduced quenching.

For ALEXA-488 (Fig. 8 B), there was a greater difference in its predicted orientation between the closed and open spHCN^{R332C} conformations. Under depolarizing conditions (Fig. 8 B, left panel), one of the highest energetically favored orientations placed the bulk of the fluorophore in the extracellular space, allowing it to form a number of contacts with the top of the VSD and thereby exhibit substantial solvent exposure. Under hyperpolarizing conditions, the fluorophore was predicted to reorientate, with the bulk of the fluorophore now buried deep within the non-polar lipid tail region (Fig. 8 B, right panel and inset). The marked difference in orientation between the two states reflects the significant voltage-dependent movements of S4, which would result in the fluorophore crossing through the juxtamembrane interface at hyperpolarizing potentials corresponding to the downward S4 helix movement. These movements would lead to a reduction of polarity in the microenvironment surrounding the fluorophore. Furthermore, ALEXA-488 was predicted to form contacts mainly with S4 itself, rather than S6, in contrast to MTS-TAMRA and consistent with ALEXA-488 reporting changes in its microenvironment closely associated with the initial rapid VSD movement.

Table 2. **Comparison of Boltzmann fit parameters before and after changing ion composition in pore**

(a) 100K solution supplemented with 10 mM CsCl

	ALEXA-488 (11)		**MTS-TAMRA (6)**	
	100K	100K+Cs	100K	100K+Cs
ΔF_{total}^{max}	1.00 ± 0.01	1.20 ± 0.03	1.00 ± 0.03	1.30 ± 0.04
$V_{0.5}{}^{F}$ (mV)	−67.8 ± 1.1	−72.2 ± 1.6	−49.7 ± 3.4	−58.2 ± 2.9
z^{F}	1.09 ± 0.05	1.27 ± 0.08	0.77 ± 0.06	0.96 ± 0.08

(b) Reducing external K^{+} from 100 mM (100K solution) to 2 mM (100Na solution)

	ALEXA-488 (5)		**MTS-TAMRA (4)**	
	100K	100Na	100K	100Na
ΔF_{total}^{max}	1.00 ± 0.01	1.10 ± 0.02	0.99 ± 0.06	1.30 ± 0.09
$V_{0.5}{}^{F}$ (mV)	−67.8 ± 0.8	−68.1 ± 1.1	−62.6 ± 5.5	−69.7 ± 6.1
z^{F}	1.08 ± 0.04	1.44 ± 0.08	0.81 ± 0.09	0.90 ± 0.12

(c) Analysis of fast component of ALEXA-488 fluorescence after supplementing with 10 mM CsCl or external K^{+} reduction.

	ALEXA-488 (9)		**ALEXA-488 (5)**	
	100K	100K+Cs	100K	100Na
ΔF_{fast}^{max}	0.62 ± 0.04	0.66 ± 0.03	0.58 ± 0.04	0.61 ± 0.04
$V_{0.5}{}^{F}$ (mV)	−90.2 ± 4.5	−88.5 ± 3.3	−80.5 ± 4.6	−81.5 ± 4.4
z^{F}	0.82 ± 0.10	0.89 ± 0.09	0.83 ± 0.12	1.02 ± 0.2

Values are shown as mean ± SE as reported by fit to pooled, normalized data using the Boltzmann equation. Data for individual cells were normalized to the control condition (100K) before pooling. Number of cells analyzed are given in parentheses. Boltzmann fit to ΔF_{fast}, normalized to ΔF_{total}^{max}. Shaded values after changing to 100K+Cs solution or 100Na solution as indicated. For ALEXA-488 labeling in c, there was no significant difference between the fit parameters of ΔF_{fast}, compared with the control (100K) (t test, $P > 0.05$) with either Cs supplement or 100K/100Na substitution.

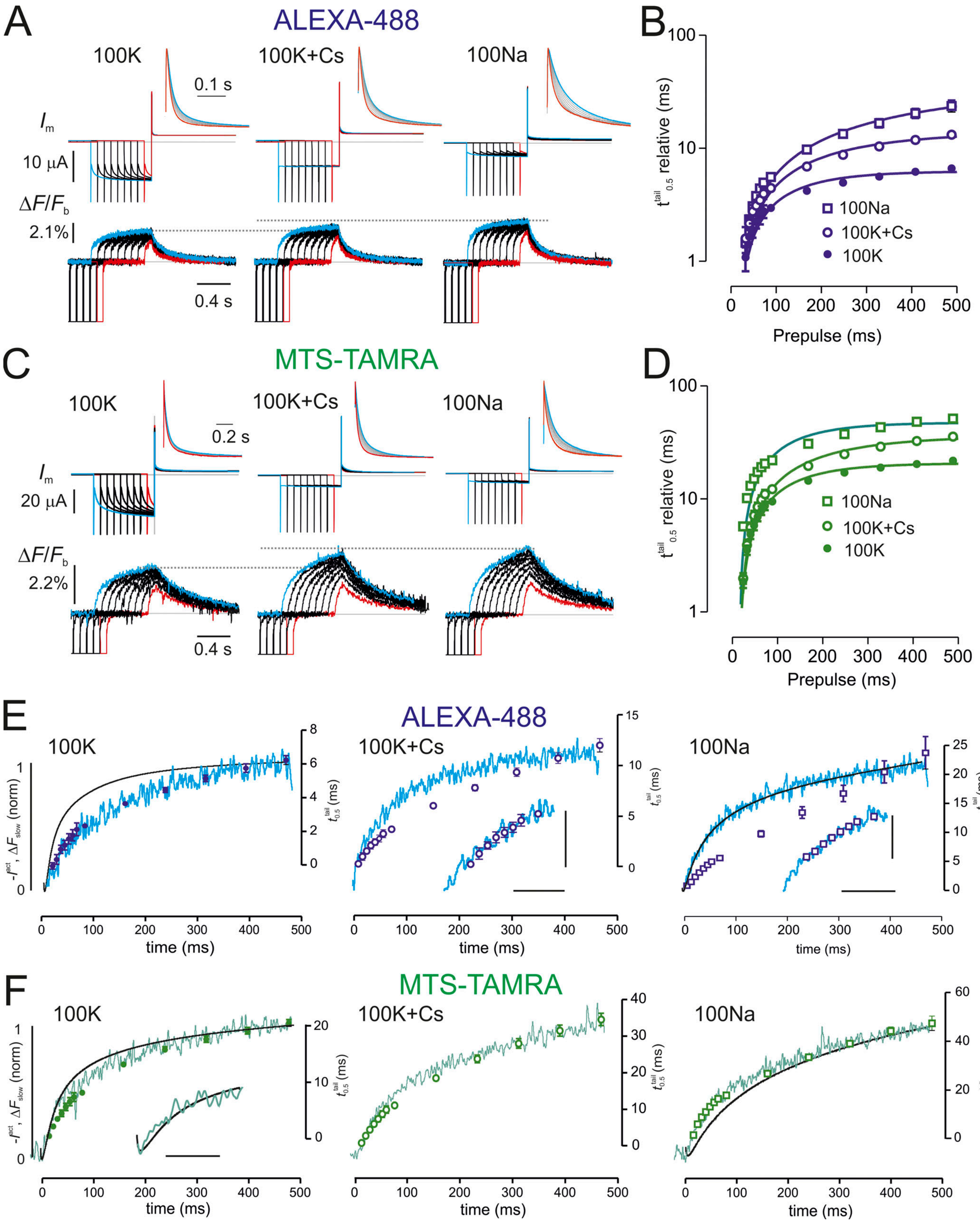

Figure 6. **Fluorescence from spHCN^{R332C} channels labeled with ALEXA-488 and MTS-TAMRA report on mode-shift development. (A)** Representative simultaneous current and ΔF recordings for an oocyte expressing spHCN^{R332C} labeled with ALEXA-488 and superfused in 100K, 100K+Cs, and 100Na solutions in response to increasing prepulse steps to −160 mV, incremented by 80 ms from an initial 8-ms wide pulse. The traces are aligned at the prepulse OFF transition to +40 mV. Insets show respective normalized tail currents at +40 mV plotted on an enlarged time scale. To resolve the tail currents, capacitive transients were eliminated by subtracting the response to the 8-ms wide pulse to −160 mV. ΔF shown as percentage of background fluorescence. Dotted lines

show that ΔF increases for superfusing with 100K+Cs and 100Na relative to 100K. The traces were signal averaged fourfold to improve the signal-to-noise ratio. ΔF shown as a percentage of background fluorescence. **(B)** Time for tail current to decay to 50% of its initial amplitude ($t_{o,5}^{tail}$) combining data with 8- and 80-ms pulse increments and shown relative to the tail response 16-ms pulse for three superfusion conditions plotted as a function of the prepulse width. Data shown as mean ± SEM, n = 10 (100K); 6 (100K+Cs); 6 (100Na). Points fitted with a single exponential function with time constants: 112 ± 12 ms (100K); 208 ± 25 ms (100K+Cs) and 490 ± 81 ms (100Na) (mean ± SE). **(C)** Representative simultaneous current and ΔF recordings for an oocyte expressing spHCN^{R332C} labeled with MTS-TAMRA, same conditions as in A. Insets show normalized tail currents as in A. ΔF shown as percentage of background fluorescence. Dotted lines show that ΔF increases for 100K+Cs and 100Na relative to the 100K condition. **(D)** Time for tail current to decay to 50% of its initial amplitude ($t_{o,5}^{tail}$) combining data with 8- and 80-ms pulse increments as in B. Data shown as mean ± SEM, n = 9 (100K); 7 (100K+Cs); 6 (100Na). Points fitted with a single exponential function with time constants: 108 ± 7 ms (100K); 173 ± 15 ms (100K+Cs) and 105 ± 7 ms (100Na) (mean ± SE). **(E)** Correlations at −160 mV between I^{act} (black trace) and the slow component of ALEXA-488 ΔF from the same cell as in A (blue trace), for superfusion conditions as indicated. I^{act} is shown inverted, and I^{act} and ΔF are normalized to corresponding values at 488 ms. Relative tail delay ($t_{o,5}^{tail}$) data from B was overlaid on the same abscissa according to the prepulse width so that the values at 16 and 488 ms match ΔF at these time points. Insets with ΔF trace expanded from 0 to100 ms, show that for 100K+Cs and 100Na at short prepulse periods (up to 88 ms) there was an improved match between the time course of ΔF and $t_{o,5}^{tail}$. Scale bars for insets: vertical 5 ms, horizontal 50 ms. **(F)** Correlations at −160 mV between I^{act} (black trace) for the slow component of MTS-TAMRA ΔF (green trace) from the same cell as in C, for superfusion conditions as indicated, plotted against time. I^{act} was inverted and ΔF normalized as in E. Inset for 100K superfusion shows an expanded view to 88 ms obtained from the same cell using the 8-ms time increment protocol with I^{act} and ΔF normalized to values at 88 ms time point. Scale bar = 40 ms. Relative tail delay ($t_{o,5}^{tail}$) data from D overlaid on the same abscissa according to the prepulse width according to the prepulse width so that the values at 16 and 488 ms match ΔF at these time points.

Discussion

Using fluorophores covalently linked to engineered cysteines in ion channels and other electrogenic membrane proteins to track conformational changes is a well-established technique that has advanced structure–function studies (Priest and Bezanilla, 2015; Cowgill and Chanda, 2019). However, there appear to be few reports in which labels with different emission/excitation properties and thiol links are compared (e.g., Gagnon et al., 2007; Gorraitz et al., 2017). The present study on the spHCN channel highlights a more general conclusion that the choice of a specific fluorophore should be considered when using VCF data to develop structure–function relations. We investigated the changes in fluorescence (ΔF) recorded from labeled spHCN channels in response to voltage steps using either ALEXA-488 or MTS-TAMRA linked to the same site in the VSD S4 helix (Cys332). Our findings using ALEXA-488 corroborate and extend those from an earlier study (Bruening-Wright et al., 2007). From the total ΔF reported by ALEXA-488, we resolved a component corresponding to the initial rapid inward movement of S4 that precedes channel opening and a component that tracked the mode shift that confers hysteresis to the channel open probability. In contrast, the slow total ΔF of MTS-TAMRA labeling could be resolved into a faster component that correlated with the early phase of channel opening and a component that tracked mode shift. Thus, despite being covalently linked to the same site, distinct aspects of S4 movement appeared to be reported by each label during channel activation. Our interpretations should be considered with caution in the light of the following caveats.

First, a potential limitation of the present study is our use of the TEVC whole oocyte configuration, whereby it is assumed that ΔF in response to voltage steps arises from a uniformly labeled population of channels that experience the same change in membrane voltage. The temporal resolution is limited by the speed of membrane charging, inhomogeneous space clamping of the oocyte resulting from the complex microstructure of the membrane, and placement of the electrodes (Baumgartner et al., 1999). Furthermore, although the electrical response arises from all expressed channels, the fluorescence signal represents the response from a subset of all labeled channels (Priest and Bezanilla, 2015), and therefore ionic current and ΔF can only be compared on an individual cell basis. Moreover, the orientation of the oocyte relative to the illumination source (inverted or non-inverted objective) might potentially result in temporal discrepancies between current and fluorescence signals. Thus the slow MTS-TAMRA response could conceivably arise from labeling inhomogeneities specific to that fluorophore and slow clamping. The technically more demanding vaseline gap/cut-open configuration (Cha and Bezanilla, 1998) would overcome these limitations and also allow gating current to be measured. It should be considered for future studies to allow more detailed correlations between ΔF and S4 movements.

Second, we report that labeling altered the gating kinetics of spHCN channels. As previously shown, the Cys substitution at R332 itself resulted in a strong left shift of the voltage dependence of spHCN channel opening, consistent with charge removal in the S4 helix (Mannikko et al., 2002). This shift was partially compensated for by labeling, and the compensatory right shift in G(V) depended on the fluorophore. These shifts in G(V) relative to the unlabeled spHCN^{R332C} are not surprising given the intrinsic charges of the fluorophores. For example, the positive partial charge of MTS-TAMRA might compensate for the loss of charge of Arg332, thereby accounting for a larger right shift, whereas ALEXA-488 has a negative partial charge due to the sulfonic groups. Thus, correlations between ΔF and channel kinetics should be interpreted with caution when relating findings to the wild type channel.

In this context, the slow ΔF reported by MTS-TAMRA labeling might also be attributable to the effect of this label on channel kinetics. Although we cannot fully exclude this without, for example, analyzing gating charge kinetics, our findings are nevertheless consistent with this response being associated with the slow, concerted S4 movement reported by the Larsson group (Wu et al., 2021). Under rate-limiting conditions (strong hyperpolarization), the fast component of current activation (τ^{I}_{fast}) was not significantly affected by either label (Fig. 2 B). Our findings that for MTS-TAMRA labeling, τ^{I}_{fast} matched the corresponding τ^{F}_{fast} closely and comparable voltage dependencies

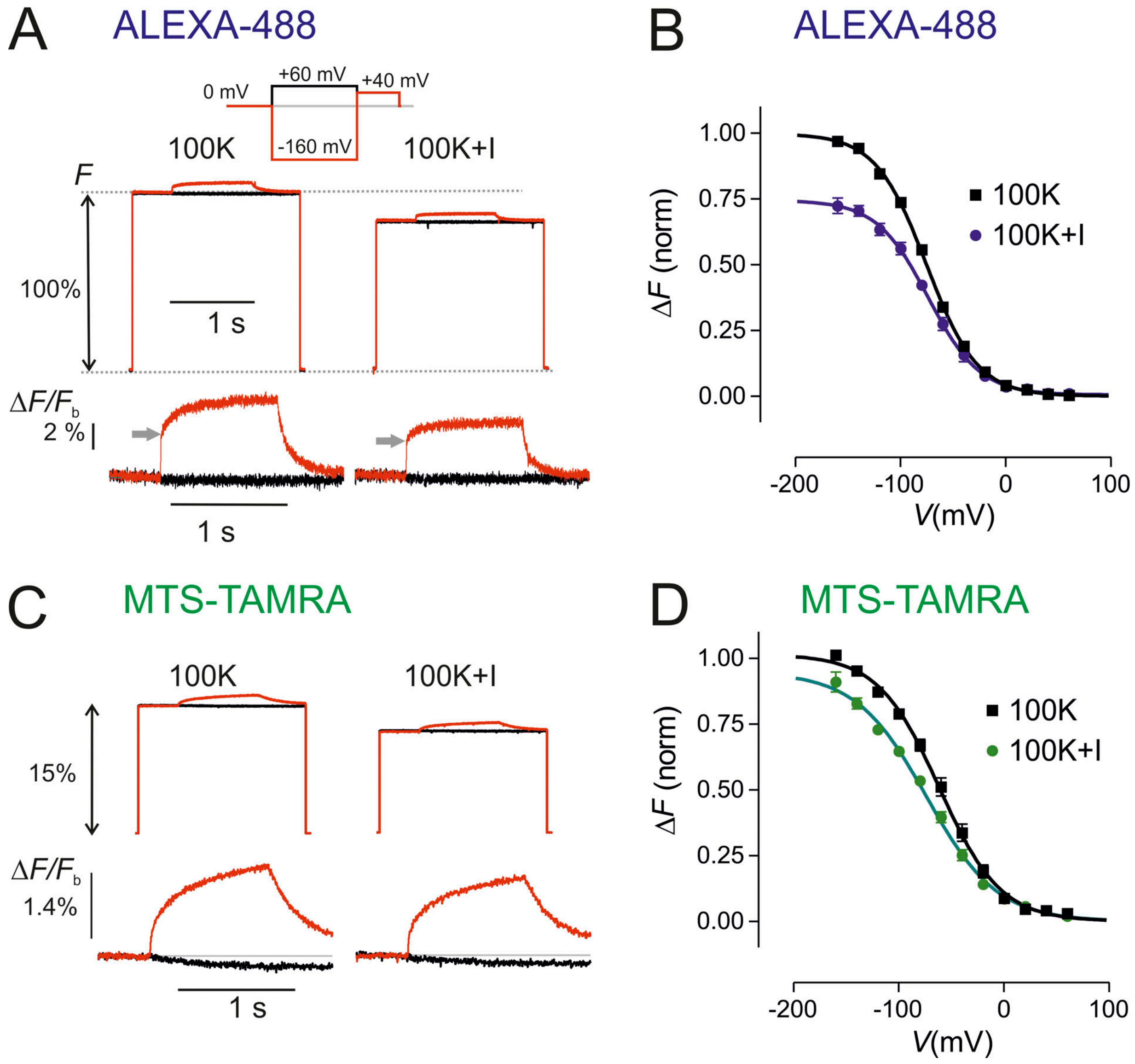

Figure 7. **Iodide quenching experiments highlight differences in solvent accessibility for each fluorophore. (A)** Recordings of ΔF under control conditions (left traces) and following incubation in a solution for 30 s supplemented with 50 mM KI (see Materials and methods) for representative ALEXA-488–labeled oocyte. Upper traces: absolute fluorescence relative to the dark state; lower traces: an expanded view of ΔF in response to a voltage step to +60 and −160 mV from 0 mV holding voltage. Arrows indicate ΔF_{fast} component that is reduced after I^- exposure (see Fig. S3). ΔF shown as percentage of background fluorescence. **(B)** ΔF_{total} plotted as a function of membrane potential pooled from (n = 9) cells and fit with the Boltzmann equation. Data were normalized to the predicted ΔF^{max}_{total} from the fit to the control data set for each cell and pooled. The fit parameters are given in Table 3. **(C)** Recordings of fluorescence under control conditions (left traces) and following incubation in a solution for 30 s supplemented with 50 mM KI (see Materials and methods) for a representative MTS-TAMRA–labeled oocyte. Upper traces: absolute fluorescence relative to the dark state; lower traces: an expanded view of ΔF in response to a voltage steps to +60 and −160 mV from 0 mV holding voltage. ΔF shown as percentage of background fluorescence. **(D)** ΔF_{total} plotted as a function of membrane potential pooled from (n = 11) cells and fit with the Boltzmann equation. Data were normalized to the predicted ΔF^{max}_{total} from the fit to the control data set for each cell and pooled. The fit parameters are given in Table 3.

were obtained for the G-V and fast ΔF-V relations (Table 1) indicated that under these conditions the labeling had not altered the kinetics of the main component of channel opening. Despite the similarities of the kinetics of channel gating and ΔF, as a general caveat, we note that drawing such direct causal links should be approached with caution without additional information on the mechanism of fluorescence quenching and the position of fluorophore relative to surrounding quenching sites (Priest and Bezanilla, 2015).

What underlies the different fluorescent responses of MTS-TAMRA and ALEX-488?

We propose that the distinctive behavior of the labels used in the present study most likely originates from the different tether lengths for ALEXA-488 and MTS-TAMRA with five and three carbon atoms, respectively. According to our docking models, this would lead to markedly different orientations of the fluorophore relative to potential quenching elements. The longer tether of ALEXA-488 would be expected to confer more

Table 3. **Comparison of Boltzmann fit parameters for spHCN^{R332C} fluorescence before and after exposure to 50 mM KI**

	ALEXA-488 (9)		**MTS-TAMRA (11)**	
	100K	**100K+KI**	**100K**	**100K+KI**
ΔF^{max}_{total}	1.00 ± 0.02	0.74 ± 0.03[a]	1.01 ± 0.02	0.95 ± 0.03
$V_{0.5}{}^F$ (mV)	−75.3 ± 1.2	−73.8 ± 2.3	−61.5 ± 2.1	−73.7 ± 2.6[a]
z^F	1.06 ± 0.05	1.05 ± 0.09	0.89 ± 0.05	0.77 ± 0.04

Values shown as mean ± SE as reported by fit to pooled, normalized data using Boltzmann equation. Number of cells analyzed given in parentheses. Data sets with iodide were normalized to ΔF^{max}_{total} for the control condition for each cell before pooling. Shaded values after iodide exposure.

[a] Indicates significant difference relative to control for each fluorophore (*t* test, $P < 0.05$).

flexibility, and therefore labeling with ALEXA-488 would have less influence on the channel kinetics as evidenced by the smaller right shift in $G(V)$ after labeling compared with MTS-TAMRA. This is corroborated by our docking analysis, which predicted that ALEXA-488 was free to undergo a significant inward movement in response to hyperpolarization, thus tracking the S4 movement. In contrast, once covalently linked to Cys332, the shorter tether of MTS-TAMRA would be expected to result in more steric constraints on the channel behavior, as evidenced by the slower deactivation kinetics and mode shift development. Our structural model of MTS-TAMRA linked to spHCN^{R332C} suggested that this fluorophore remains buried in both closed and open conformations and is in close direct contact with the pore-lining S6 helix, as well as a predicted cation–π interaction with Trp381 that may serve to stabilize its association with the S5 helix responsible for transmission of conformational changes between VSD and PD. These close contacts with S5 and S6 may serve to introduce additional friction that affects conformational transitions associated with pore closure. Its predicted pose within the spHCN protein is also consistent with the weaker I$^-$ quenching found for MTS-TAMRA labeling. In contrast, ALEXA-488 was predicted to form fewer contacts with the S6 helix and therefore may exert a weaker effect on pore closure.

ALEXA-488 reports on fast and slow VSD movement: Comparison with previous studies

Our data for ALEXA-488 labeling of Cys332 are in general agreement with those of Bruening-Wright and colleagues, whereby ΔF comprises two resolvable components (Bruening-Wright et al., 2007). They concluded that ΔF from ALEXA-488–labeled spHCN^{R332C} channels represented two distinct conformational changes of S4 that precede channel opening. ΔF from other labeled sites in S4 located closer to the N-terminal end of S4 and extracellular milieu (328–331) was similarly described by two exponential components, whereas for even more proximal sites (324–327), ΔF was best described by a single exponential (Bruening-Wright et al., 2007; Bruening-Wright and Larsson, 2007). Furthermore, ΔF correlated strongly with gating charge movement induced by voltage steps, which established that it reflected movement of S4 in response to the direction of the transmembrane electric field. The general consensus from these studies is that the faster component of ΔF represented S4 movement prior to channel opening, whereas the slower component reported the development of the mode shift following channel activation (Bruening-Wright et al., 2007; Elinder et al., 2006; Mannikko et al., 2002). Although our data appear qualitatively similar, there were differences when comparing the absolute values for time constants reported by the respective fit procedures. These might arise because the double exponential curve fitting in the earlier study was performed over a shorter time window (0.3 s, compared with 1 s in the present study). Furthermore, we used single exponential fitting procedures to resolve the components with two time windows, and signal averaging was employed for best resolution of the fast component. The fast component of ΔF using ALEXA-448 labeling was reminiscent of the rapid ΔF associated with electrochromic behavior in which the fluorophore emission is directly proportional to changes in the transmembrane electric field (Priest and Bezanilla, 2015). However, its kinetics were slower than the capacitative charging and were consistent with a voltage-dependent process associated with S4 movement. However, we cannot fully exclude an electrochromic component of ΔF without additional experiments (e.g., Dekel et al., 2012). The apparent valences (z^F) reported by fitting a two-state model to the ΔF-V (0.73 ± 0.05) and τ^F-V (0.82 ± 0.15) data sets were less than estimated from gating charge measurements (1.44 ± 0.35) reported by Bruening-Wright et al. [2007] for spHCN^{R332C}. However, the latter estimate would account for the total S4 movement comprising both fast and slow components. It should be noted that in both cases, fitting with a single Boltzmann (i.e., assuming the voltage dependence is described by a two-state model) would underestimate the true charge if multiple gating transitions are involved (Bezanilla and Villalba-Galea, 2013).

Importantly, we now report that after blocking of channels with Cs$^+$ or a 50-fold reduction in external K$^+$ (100Na solution), the voltage dependence of the fast component of ΔF reported by ALEXA-488 was only marginally affected. This was consistent with the notion that this component of S4 movement occurred independently of subsequent VSD-PD coupling initiated by the formation of a helix break in S4 (Wu et al., 2021). In contrast, the slow component of ΔF reported by ALEXA-488 was found to be sensitive to the cation composition in the pore but its estimated magnitude only deviated from the control superfusion (100K solution) for potentials at which channels began to open (i.e., below −60 mV). This indicated that the microenvironment of ALEXA-488 also reported conformational changes associated

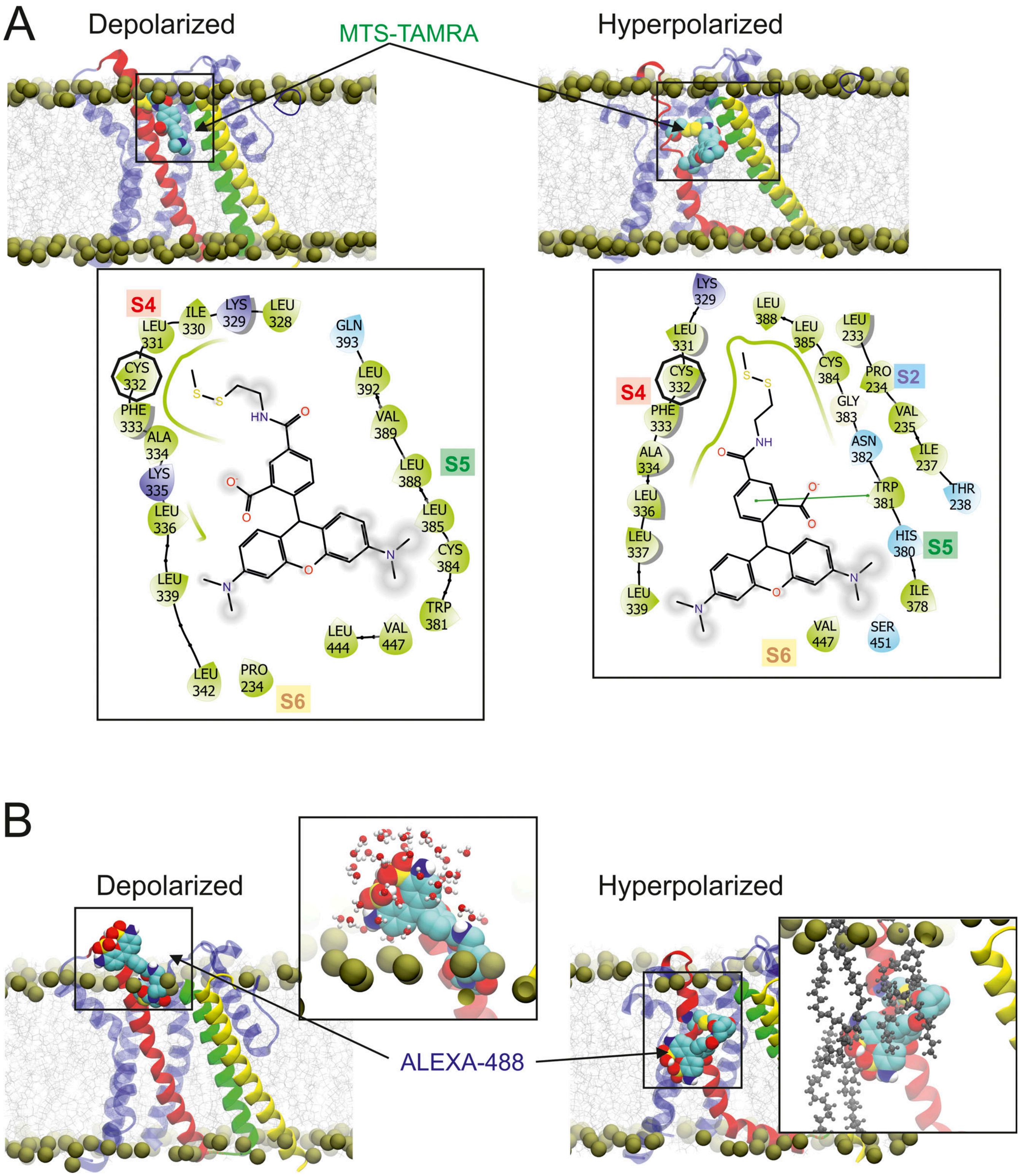

Figure 8. **Molecular structures of the postulated binding poses predicted by covalent docking calculations. (A)** MTS-TAMRA docked at depolarized spHCN^{R332C} (left) and hyperpolarized spHCN^{R332C} (right), with insets showing predicted 2-D ligand interaction diagrams. **(B)** ALEXA-488 docked at depolarized spHCN^{R332C} (left) and hyperpolarized spHCN^{R332C} (right), with insets showing close-up rendering of the fluorophore interacting with either extracellular water (left) or lipid tails (right). One subunit of spHCN^{R332C} is represented by ribbons, with S4 in red, S5 in green, and S6 in yellow. Fluorophores are shown as large brightly colored spheres, bilayer phosphorus atoms are shown in bronze to illustrate the demarcation between the water and lipid phases. For the ligand interaction diagrams, residues in green are hydrophobic, residues in blue are polar, and fluorophore atoms exposed to solvent are shown by a cloud.

with VSD to PD coupling. This may occur, for example, through the establishment of new non-covalent linkages between S4 and S5 (Bruening-Wright and Larsson, 2007; Ramentol et al., 2020; Hung et al., 2021; Wu et al., 2021; Elbahnsi et al., 2023) following the initial inward movement of the VSDs. We also note that in an earlier VCF study on the *Shaker* potassium channel with the labeling of S4, large increases in ΔF in the presence of channel blockers over the control condition were reported (Cha and Bezanilla, 1998), analogous to what we report here for spHCN^{R332C}, and were suggested by those authors to reflect initial steps leading to channel inactivation.

Recapitulation of fluorescence using a 12-state allosteric model

A 12-state allosteric scheme has been proposed (Wu et al., 2021) in which the fast ΔF was associated with the rapid, independent activation of each of the four S4s, followed by a second and concerted S4 movement that leads to channel opening at extreme hyperpolarization. In this model, states occupied after the mode shift transitions were not included. Experimental evidence for the second S4 step was obtained from fluorescence recordings using a double mutant spHCN$^{R332C/E356A}$ in which a predicted hydrogen bond between E356 at the C-terminal end of S4 and N370 in S5 is disrupted. This effectively uncouples the fast S4 movement from channel opening. ΔF from this second component correlates with G but has the opposite sign of the fast component, and it was suggested that it would be masked in the spHCN^{R332C} construct due to overlapping voltage dependencies (Wu et al., 2021). Our simulations using the same 12-state model, with parameters adjusted to fit our data, recapitulated the basic features of our ΔF recordings for each label, excluding the mode shift component (Fig. 4), and revealed how masking of the second S4 step could arise for ALEXA-488 labeling. These findings corroborated our proposal that ALEXA-488 ΔF reported an initial, rapid, and independent movement of the VSDs, together with a slower and complementary component that would correspond to the proposed concerted movement of S4 helices leading to channel opening. In contrast to ALEXA-488 labeling for which ΔF reports on both S4 steps, labeling with MTS-TAMRA resulted in a ΔF, the time course of which, appeared to track the initial phase channel activation. This would correspond to the proposed concerted movement of S4 subunits that immediately precede channel opening (Wu et al., 2021). This interpretation was recapitulated in the simulations by the close match between the voltage dependence of the simulated $G(V)$ and the simulated slow component of ΔF reported by MTS-TAMRA. In summary, our simulations were able to account for the difference in ΔF obtained under each labeling condition.

Both ALEXA-488 and MTS-TAMRA labeling report on spHCN^{R332C} mode shift

Both labels at Cys332 report a slow component of ΔF that correlated well with mode shift development. Mode shift, as evidenced by tail current delay relates to the amount of time channels are open and transition to a second mode having a different voltage dependency. This might arise in the case of HCN channels if under dynamic (non-equilibrium) conditions the energy involved in forming (activation) and subsequently breaking (deactivation) of non-covalent VSD-PD linkages is different, thereby manifesting as hysteretic behavior (Bruening-Wright and Larsson, 2007; Villalba-Galea and Chiem, 2020; Cowgill and Chanda, 2023). In general, the source of the hysteresis in channels can arise in the VSD, PD, or interdomain coupling (Villalba-Galea, 2017; Villalba-Galea and Chiem, 2020). An example of the former is the voltage-dependent phosphatase (Ci-VSP), where, using VCF, a slow component of fluorescence representing a transition to a stable, relaxed state was observed. This was hypothesized to involve the S4 segment transitioning from a 3_{10}-helix to an α-helix (Villalba-Galea et al., 2008). On the other hand, the VSD and intracellular linkers in hERG channels (Shi et al., 2020) and the selectivity filter in KscA channels (Tilegenova et al., 2017) have been implicated in determining hysteretic properties. For HCN channels, the hypothesized non-covalent linkages have yet to be identified and are directly associated with a hysteretic function.

In the presence of high (100 mM) K$^+$ in the pore, the tail current delay time course closely tracked the slow component of ΔF, although the absolute times were different for each label. This reflected the effect of the different labels on the overall channel kinetics. Furthermore, we show that blocking channels by Cs$^+$ or reducing the external K$^+$ 50-fold increased the tail current delay, and a correlation with the slow component of fluorescence was only seen for prepulse periods <100 ms. The dependence of tail current delay development on pore cation composition was not reported previously for spHCN channels (Bruening-Wright and Larsson, 2007; Elinder et al., 2006; Mannikko et al., 2005) and contrasts with the behavior found for mammalian HCN1 channels under comparable conditions (Mannikko et al., 2005). In that study, channel block by Cs$^+$ or reducing the availability of K$^+$ ions in the pore resulted in significantly faster development of tail current delay (Mannikko et al., 2005), which is the opposite of what we report here for spHCN^{R332C} channels. This may relate to differences in the pore structure between mammalian and invertebrate isoforms that alter the binding affinity of K$^+$ ions within the selectivity filter (Jackson et al., 2007; Mannikko et al., 2005).

With ALEXA-488 labeling and prepulse periods >100 ms, ΔF and $t_{0.5}^{tail}$ deviated markedly and there was greater variation in the estimates for $t_{0.5}^{tail}$ between individual oocytes. Although contamination from endogenous currents activated by the longer activation period cannot be excluded (Bruening-Wright and Larsson, 2007), the systematic dependence on the prepulse period and good agreement between ΔF and $t_{0.5}^{tail}$ with MTS-TAMRA labeling for times >100 ms under all three superfusion conditions suggests another underlying cause. For example, it may reflect the unmasking of a negative component of ΔF in the presence of 100K+Cs or 100Na observed at large hyperpolarizing potentials that would effectively reduce the mode-shift contribution to ΔF_{total}. Recently, the Larsson laboratory identified a negative ΔF under similar experimental conditions to those in our study by using the spHCN$^{R332C/E356A}$ channel to decouple the VSD and PD (Wu et al., 2021). Here, we have also documented a decrease of ΔF_{slow} with ALEXA-488 labeling at extreme hyperpolarizing potentials (Fig. 5, C and D) that may correspond to the component identified by Wu and colleagues. Further investigation of the mode shift behavior at different potentials would be required to identify the origins of the discrepancy between ΔF and $t_{0.5}^{tail}$. These experiments highlight that changes in availability of K^+ ions in the pore significantly influenced the mode shift kinetics and suggest that structural changes in the selectivity filter, which have been shown for KscA channels to alter their hysteretic properties (Tilegenova et al., 2017), also impact on the VSD movement in HCN channels. The detection of a cation-dependent mode shift in spHCN^{R332C} channels therefore validates using the sea urchin HCN channel for further studies to elucidate hysteresis as a model system.

Taken together, our study compares the responses of different fluorophores to investigate S4 movement in the HCN channel. The findings complement and extend previous VCF studies that were based exclusively on ALEXA-488 labeling from the Larsson laboratory. We provide evidence that MTS-TAMRA reports a delayed fluorescence component that may correspond to a second, concerted S4 movement that precedes channel opening. In contrast, ALEXA-488 reports both the initial, independent activation of S4 in each subunit and the concerted movement. Both probes report on the mode-shift of spHCN channels during activation, which is also dependent on the pore cation composition. Mode-shift is an important physiological mechanism for dynamically regulating rhythmicity in mammalian HCN channels, and our data highlight the use of the non-mammalian channel as a good model to investigate this biophysical property. Importantly, our study highlights how the use of different labels for VCF can potentially probe distinct biophysical aspects of ion channel opening, thereby expanding the application of VCF to investigating drug-channel interactions (e.g., Chen et al., 2022). In this context, it has been recently reported that VCF was used to track the HCN voltage sensor movement in the presence of the anesthetic and allosteric inhibitor propofol (Kim et al., 2024).

Data availability

The data are available from the corresponding author upon reasonable request.

Acknowledgments

Jeanne M. Nerbonne served as editor.

We thank Dr. Tim Karle (Florey Institute of Neuroscience and Mental Health, Parkville, Australia) for advice on the VCF hardware and for providing the excitation LEDs; and Professor Ernest Wright and Dr. Donald Loo (UCLA) for valuable comments on the manuscript and for technical discussions. The spHCN^{R332C} construct was the kind gift of Prof. H.P. Larsson (University of Linköping, Linköping, Sweden) and spHCN^{WT} was the kind gift of Prof. R. Seifert (MPINB, Bonn, Germany).

This work was supported by the Victorian State Government Operational Infrastructure Support; the Australian Government National Health and Medical Research Council (NHMRC) Independent Research Institute Infrastructure Support Scheme; an NHMRC Program Grant (10915693) (to C.A. Reid); and the Research Training Group “Chemical biology of ion channels (Chembion)” funded by the German Research Foundation, Project number: 404595355, GRK: 2515 (to M.N. Wojciechowski).

Author contributions: M.N. Wojciechowski: Formal analysis, Funding acquisition, Investigation, Resources, Writing - original draft, Writing - review & editing, C.E. McKenzie: Investigation, Resources, Writing - review & editing, A. Hung: Investigation, Methodology, Software, Visualization, Writing - original draft, Writing - review & editing, A. Kuanyshbek: Resources, Validation, Writing - review & editing, M.S. Soh: Resources, Supervision, Writing - review & editing, C.A. Reid: Conceptualization, Resources, Supervision, Writing - review & editing, I.C. Forster: Conceptualization, Data curation, Formal analysis, Investigation, Methodology, Project administration, Resources, Software, Supervision, Validation, Visualization, Writing - original draft, Writing - review & editing.

Disclosures: The authors declare no competing interests exist.

Submitted: 2 February 2024
Revised: 17 May 2024
Accepted: 11 June 2024

References

Altomare, C., A. Bucchi, E. Camatini, M. Baruscotti, C. Viscomi, A. Moroni, and D. DiFrancesco. 2001. Integrated allosteric model of voltage gating of HCN channels. *J. Gen. Physiol.* 117:519–532. https://doi.org/10.1085/jgp.117.6.519

Baumgartner, W., L. Islas, and F.J. Sigworth. 1999. Two-microelectrode voltage clamp of Xenopus oocytes: Voltage errors and compensation for local current flow. *Biophys. J.* 77:1980–1991. https://doi.org/10.1016/S0006-3495(99)77039-6

Bezanilla, F., and C.A. Villalba-Galea. 2013. The gating charge should not be estimated by fitting a two-state model to a Q-V curve. *J. Gen. Physiol.* 142:575–578. https://doi.org/10.1085/jgp.201311056

Bianco, G., S. Forli, D.S. Goodsell, and A.J. Olson. 2016. Covalent docking using autodock: Two-point attractor and flexible side chain methods. *Protein Sci.* 25:295–301. https://doi.org/10.1002/pro.2733

Biel, M., C. Wahl-Schott, S. Michalakis, and X. Zong. 2009. Hyperpolarization-activated cation channels: From genes to function. *Physiol. Rev.* 89:847–885. https://doi.org/10.1152/physrev.00029.2008

Bruening-Wright, A., F. Elinder, and H.P. Larsson. 2007. Kinetic relationship between the voltage sensor and the activation gate in spHCN channels. *J. Gen. Physiol.* 130:71–81. https://doi.org/10.1085/jgp.200709769

Bruening-Wright, A., and H.P. Larsson. 2007. Slow conformational changes of the voltage sensor during the mode shift in hyperpolarization-activated cyclic-nucleotide-gated channels. *J. Neurosci.* 27:270–278. https://doi.org/10.1523/JNEUROSCI.3801-06.2007

Burtscher, V., J. Mount, J. Huang, J. Cowgill, Y. Chang, K. Bickel, J. Chen, P. Yuan, and B. Chanda. 2024. Structural basis for hyperpolarization-dependent opening of human HCN1 channel. *Nat. Commun.* 15:5216. https://doi.org/10.1038/s41467-024-49599-x

Cha, A., and F. Bezanilla. 1998. Structural implications of fluorescence quenching in the Shaker K+ channel. *J. Gen. Physiol.* 112:391–408. https://doi.org/10.1085/jgp.112.4.391

Chen, L., G. Peng, T.W. Comollo, X. Zou, K.J. Sampson, H.P. Larsson, and R.S. Kass. 2022. Two small-molecule activators share similar effector sites in the KCNQ1 channel pore but have distinct effects on voltage sensor movements. *Front. Physiol.* 13:903050. https://doi.org/10.3389/fphys.2022.903050

Clark, M.D., G.F. Contreras, R. Shen, and E. Perozo. 2020. Electromechanical coupling in the hyperpolarization-activated K^+ channel KAT1. *Nature.* 583:145–149. https://doi.org/10.1038/s41586-020-2335-4

Cowgill, J., and B. Chanda. 2019. The contribution of voltage clamp fluorometry to the understanding of channel and transporter mechanisms. *J. Gen. Physiol.* 151:1163–1172. https://doi.org/10.1085/jgp.201912372

Cowgill, J., and B. Chanda. 2023. Charge-voltage curves of Shaker potassium channel are not hysteretic at steady state. *J. Gen. Physiol.* 155:e202112883. https://doi.org/10.1085/jgp.202112883

Cowgill, J., V.A. Klenchin, C. Alvarez-Baron, D. Tewari, A. Blair, and B. Chanda. 2019. Bipolar switching by HCN voltage sensor underlies hyperpolarization activation. *Proc. Natl. Acad. Sci. USA*. 116:670–678. https://doi.org/10.1073/pnas.1816724116

Dai, G., T.K. Aman, F. DiMaio, and W.N. Zagotta. 2019. The HCN channel voltage sensor undergoes a large downward motion during hyperpolarization. *Nat. Struct. Mol. Biol.* 26:686–694. https://doi.org/10.1038/s41594-019-0259-1

Dallakyan, S., and A.J. Olson. 2015. Small-molecule library screening by docking with PyRx. *Methods Mol. Biol.* 1263:243–250. https://doi.org/10.1007/978-1-4939-2269-7_19

Dekel, N., M.F. Priest, H. Parnas, I. Parnas, and F. Bezanilla. 2012. Depolarization induces a conformational change in the binding site region of the M2 muscarinic receptor. *Proc. Natl. Acad. Sci. USA*. 109:285–290. https://doi.org/10.1073/pnas.1119424109

Eberhardt, J., D. Santos-Martins, A.F. Tillack, and S. Forli. 2021. AutoDock Vina 1.2.0: New docking methods, expanded force field, and Python bindings. *J. Chem. Inf. Model.* 61:3891–3898. https://doi.org/10.1021/acs.jcim.1c00203

Elbahnsi, A., J. Cowgill, V. Burtscher, L. Wedemann, L. Zeckey, B. Chanda, and L. Delemotte. 2023. Interplay between VSD, pore, and membrane lipids in electromechanical coupling in HCN channels. *Elife*. 12:e80303. https://doi.org/10.7554/eLife.80303

Elinder, F., R. Männikkö, S. Pandey, and H.P. Larsson. 2006. Mode shifts in the voltage gating of the mouse and human HCN2 and HCN4 channels. *J. Physiol.* 575:417–431. https://doi.org/10.1113/jphysiol.2006.110437

Flynn, G.E., and W.N. Zagotta. 2018. Insights into the molecular mechanism for hyperpolarization-dependent activation of HCN channels. *Proc. Natl. Acad. Sci. USA*. 115:E8086–E8095. https://doi.org/10.1073/pnas.1805596115

Fryatt, A.G., and R.J. Evans. 2014. Kinetics of conformational changes revealed by voltage-clamp fluorometry give insight to desensitization at ATP-gated human P2X1 receptors. *Mol. Pharmacol.* 86:707–715. https://doi.org/10.1124/mol.114.095307

Gagnon, D.G., C. Frindel, and J.Y. Lapointe. 2007. Voltage-clamp fluorometry in the local environment of the C255-C511 disulfide bridge of the Na+/glucose cotransporter. *Biophys. J.* 92:2403–2411. https://doi.org/10.1529/biophysj.106.097964

Gauss, R., R. Seifert, and U.B. Kaupp. 1998. Molecular identification of a hyperpolarization-activated channel in sea urchin sperm. *Nature*. 393:583–587. https://doi.org/10.1038/31248

Gorraitz, E., B.A. Hirayama, A. Paz, E.M. Wright, and D.D.F. Loo. 2017. Active site voltage clamp fluorometry of the sodium glucose cotransporter hSGLT1. *Proc. Natl. Acad. Sci. USA*. 114:E9980–E9988. https://doi.org/10.1073/pnas.1713899114

Hung, A., I.C. Forster, C.E. Mckenzie, G. Berecki, S. Petrou, A. Kathirvel, M.S. Soh, and C.A. Reid. 2021. Biophysical analysis of an HCN1 epilepsy variant suggests a critical role for S5 helix Met-305 in voltage sensor to pore domain coupling. *Prog. Biophys. Mol. Biol.* 166:156–172. https://doi.org/10.1016/j.pbiomolbio.2021.07.005

Jackson, H.A., C.R. Marshall, and E.A. Accili. 2007. Evolution and structural diversification of hyperpolarization-activated cyclic nucleotide-gated channel genes. *Physiol. Genomics*. 29:231–245. https://doi.org/10.1152/physiolgenomics.00142.2006

Kasimova, M.A., D. Tewari, J.B. Cowgill, W.C. Ursuleaz, J.L. Lin, L. Delemotte, and B. Chanda. 2019. Helix breaking transition in the S4 of HCN channel is critical for hyperpolarization-dependent gating. *Elife*. 8:e53400. https://doi.org/10.7554/eLife.53400

Kim, E.D., X. Wu, S. Lee, G.R. Tibbs, K.P. Cunningham, M.E. Perez, P.A. Goldstein, A. Accardi, P.H. Larsson, and C.M. Nimigean. 2024. Propofol rescues HCN1 epilepsy mutants and reveals non-canonical voltage-dependent gating in HCN channels. *Nature*. In press.

Lee, C.H., and R. MacKinnon. 2017. Structures of the human HCN1 hyperpolarization-activated channel. *Cell*. 168:111–120.e11. https://doi.org/10.1016/j.cell.2016.12.023

Lee, C.H., and R. MacKinnon. 2019. Voltage sensor movements during hyperpolarization in the HCN channel. *Cell*. 179:1582–1589.e7. https://doi.org/10.1016/j.cell.2019.11.006

Loo, D.D., B.A. Hirayama, A. Cha, F. Bezanilla, and E.M. Wright. 2005. Perturbation analysis of the voltage-sensitive conformational changes of the Na+/glucose cotransporter. *J. Gen. Physiol.* 125:13–36. https://doi.org/10.1085/jgp.200409150

Ludwig, A., X. Zong, M. Jeglitsch, F. Hofmann, and M. Biel. 1998. A family of hyperpolarization-activated mammalian cation channels. *Nature*. 393:587–591. https://doi.org/10.1038/31255

Männikkö, R., F. Elinder, and H.P. Larsson. 2002. Voltage-sensing mechanism is conserved among ion channels gated by opposite voltages. *Nature*. 419:837–841. https://doi.org/10.1038/nature01038

Männikkö, R., S. Pandey, H.P. Larsson, and F. Elinder. 2005. Hysteresis in the voltage dependence of HCN channels: Conversion between two modes affects pacemaker properties. *J. Gen. Physiol.* 125:305–326. https://doi.org/10.1085/jgp.200409130

Mannuzzu, L.M., and E.Y. Isacoff. 2000. Independence and cooperativity in rearrangements of a potassium channel voltage sensor revealed by single subunit fluorescence. *J. Gen. Physiol.* 115:257–268. https://doi.org/10.1085/jgp.115.3.257

Mannuzzu, L.M., M.M. Moronne, and E.Y. Isacoff. 1996. Direct physical measure of conformational rearrangement underlying potassium channel gating. *Science*. 271:213–216. https://doi.org/10.1126/science.271.5246.213

McKenzie, C.E., A. Hung, A.M. Phillips, M.S. Soh, C.A. Reid, and I.C. Forster. 2023. The potential antidepressant compound org 34167 modulates HCN channels via a novel mode of action. *Mol. Pharmacol.* 104:62–72. https://doi.org/10.1124/molpharm.123.000676

Morris, G.M., R. Huey, W. Lindstrom, M.F. Sanner, R.K. Belew, D.S. Goodsell, and A.J. Olson. 2009. AutoDock4 and AutoDockTools4: Automated docking with selective receptor flexibility. *J. Comput. Chem.* 30:2785–2791. https://doi.org/10.1002/jcc.21256

Papp, F., G.E.S. Toombes, Z. Pethő, A. Bagosi, A. Feher, J. Almássy, J. Borrego, Á. Kuki, S. Kéki, G. Panyi, and Z. Varga. 2022. Multiple mechanisms contribute to fluorometry signals from the voltage-gated proton channel. *Commun. Biol.* 5:1131. https://doi.org/10.1038/s42003-022-04065-6

Pathak, M.M., V. Yarov-Yarovoy, G. Agarwal, B. Roux, P. Barth, S. Kohout, F. Tombola, and E.Y. Isacoff. 2007. Closing in on the resting state of the Shaker K(+) channel. *Neuron*. 56:124–140. https://doi.org/10.1016/j.neuron.2007.09.023

Patti, M., C. Fenollar-Ferrer, A. Werner, L.R. Forrest, and I.C. Forster. 2016. Cation interactions and membrane potential induce conformational changes in NaPi-IIb. *Biophys. J.* 111:973–988. https://doi.org/10.1016/j.bpj.2016.07.025

Patti, M., and I.C. Forster. 2014. Correlating charge movements with local conformational changes of a Na(+)-coupled cotransporter. *Biophys. J.* 106:1618–1629. https://doi.org/10.1016/j.bpj.2014.02.028

Priest, M., and F. Bezanilla. 2015. Functional site-directed fluorometry. *Adv. Exp. Med. Biol.* 869:55–76. https://doi.org/10.1007/978-1-4939-2845-3_4

Ramentol, R., M.E. Perez, and H.P. Larsson. 2020. Gating mechanism of hyperpolarization-activated HCN pacemaker channels. *Nat. Commun.* 11:1419. https://doi.org/10.1038/s41467-020-15233-9

Shi, Y.P., S. Thouta, and T.W. Claydon. 2020. Modulation of hERG K^+ channel deactivation by voltage sensor relaxation. *Front. Pharmacol.* 11:139. https://doi.org/10.3389/fphar.2020.00139

Sørensen, J.B., A. Cha, R. Latorre, E. Rosenman, and F. Bezanilla. 2000. Deletion of the S3-S4 linker in the Shaker potassium channel reveals two quenching groups near the outside of S4. *J. Gen. Physiol.* 115:209–222. https://doi.org/10.1085/jgp.115.2.209

Tilegenova, C., D.M. Cortes, and L.G. Cuello. 2017. Hysteresis of KcsA potassium channel's activation- deactivation gating is caused by structural changes at the channel's selectivity filter. *Proc. Natl. Acad. Sci. USA*. 114:3234–3239. https://doi.org/10.1073/pnas.1618101114

Trott, O., and A.J. Olson. 2010. AutoDock Vina: Improving the speed and accuracy of docking with a new scoring function, efficient optimization, and multithreading. *J. Comput. Chem.* 31:455–461. https://doi.org/10.1002/jcc.21334

Villalba-Galea, C.A. 2017. Hysteresis in voltage-gated channels. *Channels*. 11:140–155. https://doi.org/10.1080/19336950.2016.1243190

Villalba-Galea, C.A., and A.T. Chiem. 2020. Hysteretic behavior in voltage-gated channels. *Front. Pharmacol.* 11:579596. https://doi.org/10.3389/fphar.2020.579596

Villalba-Galea, C.A., W. Sandtner, D.M. Starace, and F. Bezanilla. 2008. S4-based voltage sensors have three major conformations. *Proc. Natl. Acad. Sci. USA*. 105:17600–17607. https://doi.org/10.1073/pnas.0807387105

Virkki, L.V., H. Murer, and I.C. Forster. 2006. Mapping conformational changes of a type IIb Na+/Pi cotransporter by voltage clamp fluorometry. *J. Biol. Chem.* 281:28837–28849. https://doi.org/10.1074/jbc.M603861200

Wahl-Schott, C., L. Baumann, X. Zong, and M. Biel. 2005. An arginine residue in the pore region is a key determinant of chloride dependence in cardiac pacemaker channels. *J. Biol. Chem.* 280:13694–13700. https://doi.org/10.1074/jbc.M413197200

Wahl-Schott, C., and M. Biel. 2009. HCN channels: Structure, cellular regulation and physiological function. *Cell. Mol. Life Sci.* 66:470–494. https://doi.org/10.1007/s00018-008-8525-0

Wang, W., and R. MacKinnon. 2017. Cryo-EM structure of the open human Ether-à-go-go-related K$^+$ channel hERG. *Cell*. 169:422–430.e10. https://doi.org/10.1016/j.cell.2017.03.048

Waterhouse, A., M. Bertoni, S. Bienert, G. Studer, G. Tauriello, R. Gumienny, F.T. Heer, T.A.P. de Beer, C. Rempfer, L. Bordoli, et al. 2018. SWISS-MODEL: Homology modelling of protein structures and complexes. *Nucleic Acids Res*. 46:W296–W303. https://doi.org/10.1093/nar/gky427

Wu, X., K.P. Cunningham, R. Ramentol, M.E. Perez, and H.P. Larsson. 2023. Similar voltage-sensor movement in spHCN channels can cause closing, opening, or inactivation. *J. Gen. Physiol.* 155:e202213170. https://doi.org/10.1085/jgp.202213170

Wu, X., R. Ramentol, M.E. Perez, S.Y. Noskov, and H.P. Larsson. 2021. A second S4 movement opens hyperpolarization-activated HCN channels. *Proc. Natl. Acad. Sci. USA*. 118:e2102036118. https://doi.org/10.1073/pnas.2102036118

Zhang, Y., S. Forli, A. Omelchenko, and M.F. Sanner. 2019. AutoGridFR: Improvements on AutoDock affinity maps and associated software tools. *J. Comput. Chem.* 40:2882–2886. https://doi.org/10.1002/jcc.26054

Supplemental material

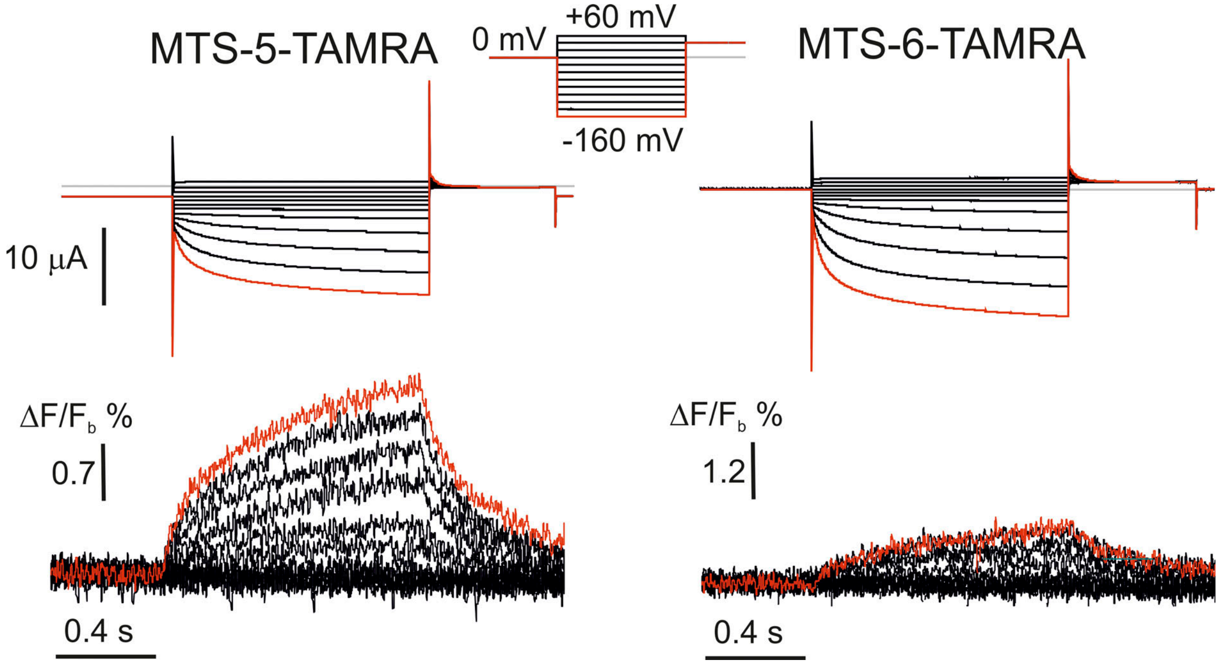

Figure S1. **Labeling spHCN^{R332C} with single isomers MTS-5-TAMRA and MTS-6-TAMRA recapitulates the mixed isomer response.** Response of representative oocytes expressing spHCN^{R332C} and labeled with either MTS-5-TAMRA (left) or MTS-6-TAMRA (right) to the voltage step protocol shown in the inset. Upper traces: membrane current; lower traces: fluorescence. Oocytes were labeled under the same conditions as for the mixed isomer (see Materials and methods) and were from the same donor frog.

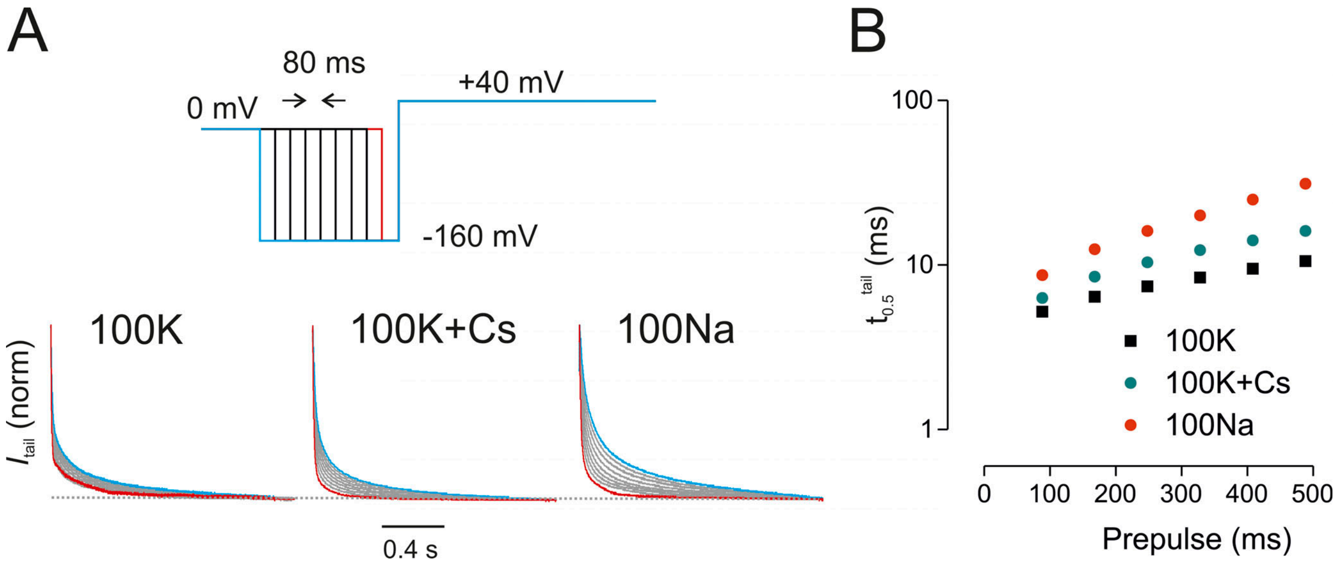

Figure S2. **Mode shift as evidenced by tail current delay was also observed for unlabeled spHCN^{R332C}. (A)** Normalized tail currents from a representative unlabeled cell expressing spHCN^{R332C} shown for three superfusion conditions as indicated using the voltage step protocol shown in the inset with 80-ms increments in prepulse to −160 mV. **(B)** Tail current delay, quantified as time to 50% of initial amplitude relative to 8 ms, plotted as a function of prepulse width for each superfusion condition.

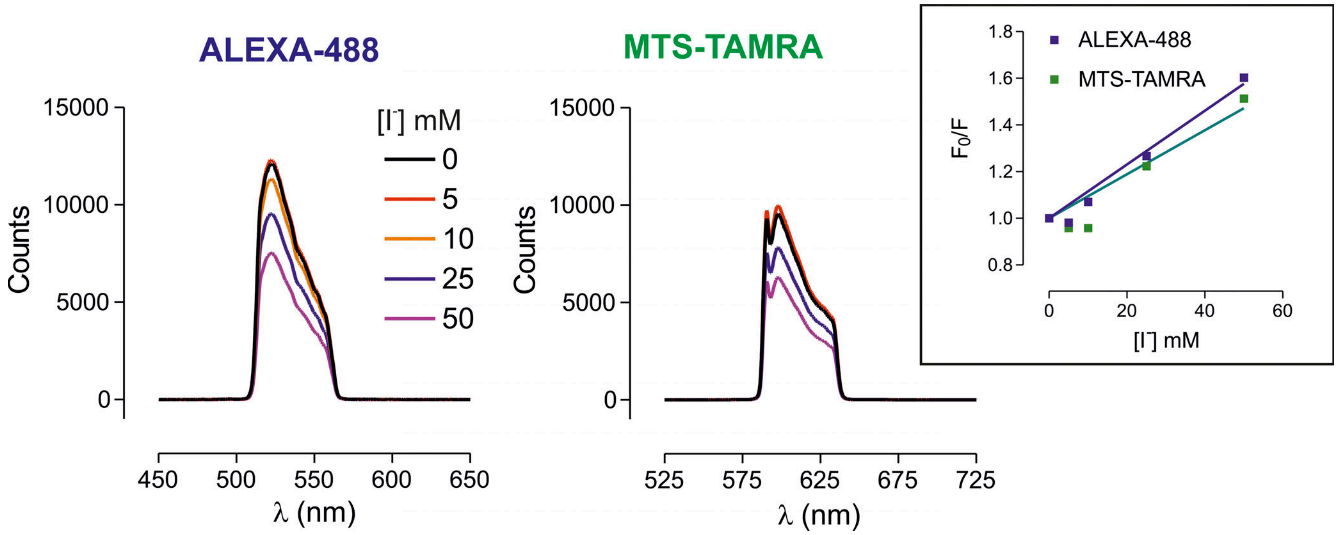

Figure S3. **Iodide quenching of fluorophores in solution.** Spectrum of ALEXA-448 (left) and MTS-TAMRA (right) for different iodide concentrations. Each measurement was made from a 2 µl drop of solution containing the fluorophore (5 µM) and the iodide concentration indicated (see Materials and methods). The same optical components were used as for the recordings with labeled oocytes. LED current was set to 200 and 400 mA for ALEXA-488 and MTS-TAMRA, respectively. Inset shows Stern–Volmer plots for normalized spectral peaks. Straight lines are linear regression fits, forced to origin at $F_0/F = 1.0$, where F_0 is the control ($[I^-] = 0$) peak fluorescence count and F is the value at the same wavelength for a given $[I^-]$. The Stern–Volmer quenching constants were 0.012 ± 0.001 mM^{-1} (ALEXA-488) and 0.009 ± 0.002 mM^{-1} (MTS-TAMRA), indicating comparable quenching effects.

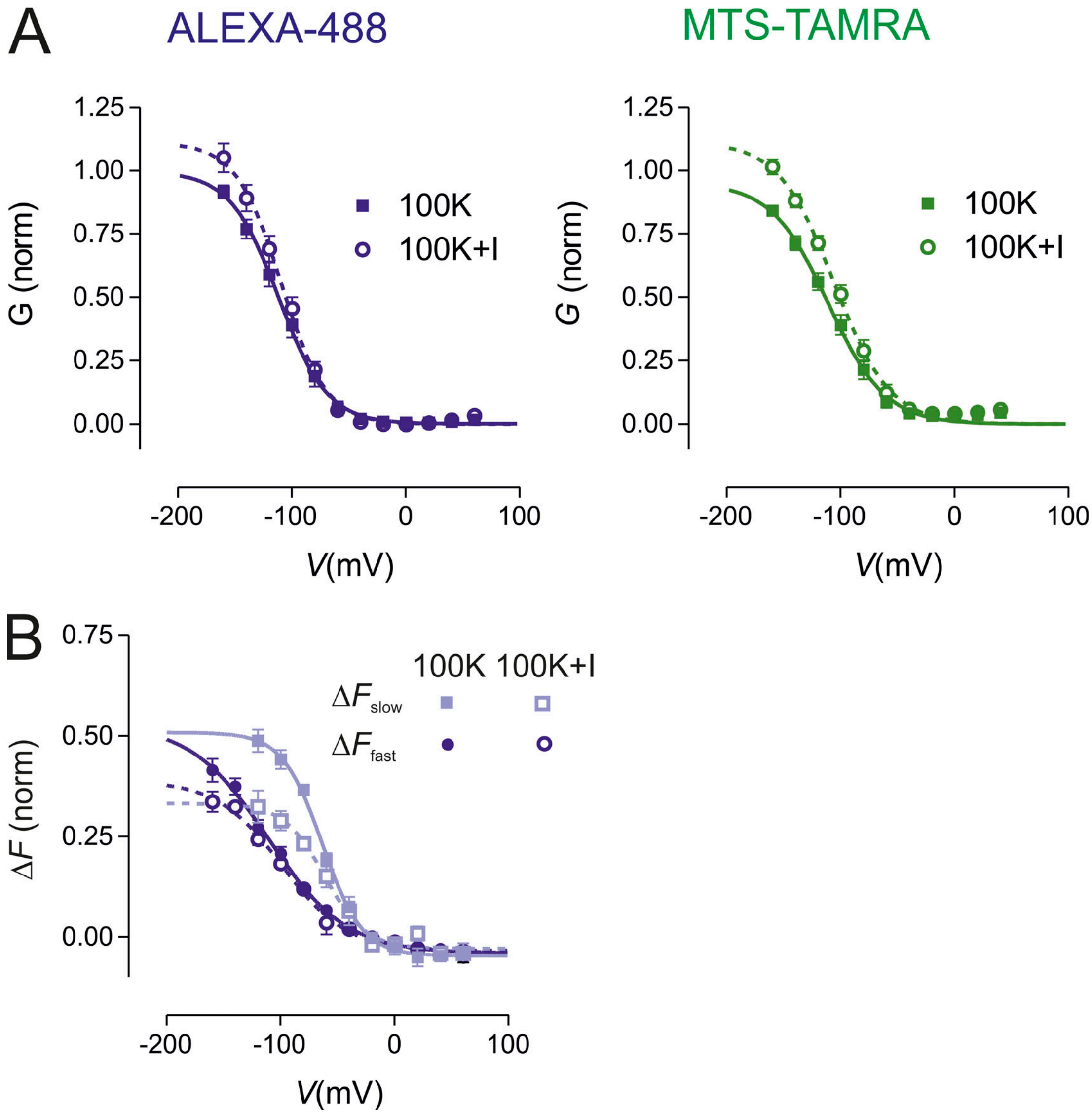

Figure S4. **Normalized conductance increases during exposure to I⁻ without affecting voltage dependence. (A)** Normalized conductance (G_{norm}) plotted as a function of voltage for spHCN^{R332C}-expressing oocytes before (100K) and after exposure to 50 mM KI (100K+I) and labeled with ALEXA-488 (left) or MTS-TAMRA (right). Conductance was determined from tail currents in response to 1 s voltage steps using standard activation protocol (see Fig. 1 and Materials and methods). Data for individual cells were normalized to maximum conductance for the control (100K) condition, determined from a Boltzmann fit. Data points show mean ± SEM (*n* = 4) for each label. Fit parameters are given in Table S2. **(B)** Components of Δ*F* for ALEXA-488 labeling before (100K) and after exposure to I⁻ (100K+I) obtained by fitting Δ*F*–*V* data to a single exponential with variable offset (see text). Each component was normalized to ΔF^{max}_{total} for each cell and pooled. Continuous lines are fits using Boltzmann function to data. Fit parameters are given in Table S3.

Provided online are three tables. Table S1 shows simulation parameters. Table S2 shows fit parameters for fitting normalized conductance before and after I⁻ exposure. Table S3 shows fit parameters for fitting Δ*F*-*V* data before and after I⁻ exposure.